

1 **Distinctive aerosol-cloud-precipitation interactions in marine boundary layer clouds from the**
2 **ACE-ENA and SOCRATES aircraft field campaigns**

3
4 Xiaojian Zheng^{1,a}, Xiquan Dong¹, Baike Xi¹, Timothy Logan² and Yuan Wang³

5
6 ¹Department of Hydrology and Atmospheric Sciences, University of Arizona, Tucson, AZ, USA

7 ²Department of Atmospheric Sciences, Texas A&M University, College Station, TX, USA

8 ³Department of Earth System Sciences, Stanford University, Stanford, CA, USA

9 ^aNow at: Environmental Science Division, Argonne National Laboratory, Lemont, IL, USA

10
11 **Correspondence:** Xiquan Dong (xdong@arizona.edu)

12
13 **Abstract.** The aerosol-cloud-precipitation interactions within the cloud-topped Marine Boundary Layer
14 (MBL) are examined using aircraft in-situ measurements from Aerosol and Cloud Experiments in the
15 Eastern North Atlantic (ACE-ENA) and Southern Ocean Clouds Radiation Aerosol Transport
16 Experimental Study (SOCRATES) field campaigns. SOCRATES clouds exhibit a larger number
17 concentration and smaller cloud droplet effective radius (148.3 cm⁻³ and 8.0 μm) compared to ACE-ENA
18 summertime (89.4 cm⁻³ and 9.0 μm) and wintertime clouds (70.6 cm⁻³ and 9.8 μm). The ACE-ENA clouds,
19 especially during the winter, feature stronger drizzle formation via droplet growth through enhanced
20 collision-coalescence, attributed to a relatively cleaner environment and deeper cloud layer. Furthermore,
21 the Aerosol-Cloud Interaction (ACI) indices from the two aircraft field campaigns exhibit distinct
22 sensitivities, indicating different cloud microphysical responses to aerosols. The ACE-ENA winter
23 season features relatively fewer aerosols, which are more likely activated into cloud droplets under the
24 conditions of sufficient water vapor availability and strong turbulence. The enriched aerosol loading
25 during ACE-ENA summer and SOCRATES generally leads to smaller cloud droplets competing for the

Deleted: being

Deleted: have

Deleted: droplets

Deleted: in wintertime, exhibit

Deleted: and

Deleted: due to

Deleted: the

Deleted: suggest

Deleted: the

Deleted: reside in different regimes. Aerosols during

Deleted: to be

Deleted: , given the aerosol-limited regime

Deleted: available

39 ~~limited~~ water vapor and exhibiting a stronger ACI. Notably, the precipitation susceptibilities are ~~stronger~~
40 during the ACE-ENA than during the SOCRATES campaigns. The in-cloud drizzle ~~behavior~~
41 significantly ~~alters~~ sub-cloud cloud condensation nuclei (CCN) budgets through the coalescence-
42 scavenging effect, and in turn, impact the ACI assessments. The results of this study can enhance the
43 understanding and aid in future model simulation and assessment of the aerosol-cloud interaction.

Deleted: in the water-vapor-limit regime.

Deleted: more pronounced

Deleted: evolutions

Deleted: alter

46 1. Introduction

47 Marine boundary layer (MBL) clouds substantially impact the Earth's climate system (Dong and
48 Minnis, 2022). Sustained by large-scale subsidence and cloud-top longwave radiative cooling, MBL
49 clouds, typically located beneath the temperature inversion at the MBL top, persistently reflect the
50 incoming solar radiation and modulate the radiative balance (Lilly, 1968; Albrecht et al., 1995; Wood et
51 al., 2015; Dong et al., 2023). The climatic significance of MBL cloud radiative effects, which remains
52 largely uncertain (IPCC, 2022), is closely linked to cloud microphysical properties that are substantially
53 influenced by surrounding aerosol conditions (Chen et al., 2014; Feingold and McComiskey, 2016).
54 Observational evidence demonstrates that cloud microphysical responses to aerosols, defined as the
55 aerosol-cloud interaction (ACI), can be typically viewed as decreased cloud droplet effective radii (r_c)
56 and increased number concentrations (N_c) with more aerosol intrusion under conditions of comparable
57 cloud water content (Feingold and McComiskey, 2016). The ACIs have been extensively investigated
58 by different observational platforms, such as aircraft (Hill et al., 2009; Diamond et al., 2018; Gupta et
59 al., 2022), ground-based and satellite observations (Painemal et al., 2020; Zhang et al., 2022; Zheng et
60 al., 2022a), and model simulations (Wang et al., 2020; Christensen et al., 2023) over different maritime
61 regions like the southeast Pacific (Painemal and Zuidema, 2011), northeast Pacific (Braun et al., 2018),
62 southeast Atlantic (Gupta et al., 2022), and eastern North Atlantic (Zheng et al., 2022a).

67 Furthermore, ~~a larger number of small~~ cloud droplets ~~can sometimes~~ extend cloud longevity and
68 spatial coverage ~~and~~ modulate the precipitation processes ~~in the MBL clouds~~, reflecting the cloud
69 adjustments to aerosol disturbances (Albrecht, 1989; Bellouin et al., 2020). Precipitation, particularly in
70 the form of drizzle, is common in MBL clouds (Wood et al., 2015; Wu et al., 2020), and the turbulence
71 forced by stratocumulus cloud-top radiative cooling can increase the cloud liquid water path and
72 contribute to drizzle production (Ghate et al., 2019, 2021). The drizzle formation and growth processes
73 are deeply entwined with the MBL aerosols and dynamics. ~~Frequent aerosol intrusions in the MBL~~ have
74 been found to ~~have to lower the efficiency of collision-coalescence-induced which results in the~~
75 ~~suppression of~~ precipitation frequency and strength. ~~Such phenomenon can be quantified and assessed~~
76 via ~~the~~ cloud precipitation susceptibility (Feingold and Seibert, 2009; Lu et al., 2009; Sorooshian et al.,
77 2009; Duong et al., 2011). ~~The~~ assessments of precipitation susceptibility are examined to be under the
78 influences of methodology (Terai et al., 2012), cloud morphology (Sorooshian et al., 2009; Jung et al.,
79 2016), ambient aerosol concentrations (Duong et al., 2011; Jung et al., 2016; Gupta et al., 2022), and
80 cloud thickness (Terai et al., 2012; Jung et al., 2016; Gupta et al., 2022). The in-cloud turbulence and
81 wind shear can effectively enhance collision-coalescence efficiency, ~~stimulate~~ drizzle formation and
82 growth, and consequently ~~lead~~ to enhanced precipitation ~~rate and amount~~ (Chen et al., 2011; Wu et al.,
83 2017). Cloud-top entrainment of dryer and warmer air can potentially deplete small cloud droplets and
84 shrink large droplets via evaporation, thereby impacting cloud~~top~~ microphysical processes depending
85 on the homogeneous or inhomogeneous mixing regimes (Lehmann et al., 2009; Jia et al., 2019).

86 Conversely, precipitation has been shown to exert a substantial influence on the MBL aerosol and
87 cloud condensation nuclei (CCN) budget through the coalescence-scavenging effect. The coalescence-
88 scavenging refers to the process in which cloud or drizzle droplets, containing aerosol particles inside,
89 merge with each other. Upon the collision-coalescence of cloud droplets, the dissolved aerosol masses
90 within the cloud droplets also collide and merge into a larger aerosol core, leading to larger aerosol
91 particles upon droplet evaporation. The sub-cloud aerosols are then replenished into the cloud layer,

Deleted: more and smaller

Deleted: not only

Deleted: but also

Deleted: Aerosols

Deleted: suppress the

Deleted: by constantly buffering cloud droplet number concentrations...

Deleted: activation, hence increasing

Deleted: Furthermore, the

Deleted: stimulating

Deleted: leading

Deleted:

104 experiencing growth within the cloud through cloud and drizzle droplet collision-coalescence and
105 subsequently falling and evaporating outside the cloud again. Eventually, the residual aerosols
106 undergoing this cloud-processing cycle will gradually decrease in number concentration and increase in
107 size (Flossmann et al., 1985; Feingold et al., 1996; Hudson and Noble, 2020; Hoffmann and Feingold,
108 2023). In addition, the drizzle drops, ~~upon~~ falling out of the cloud base, can result in net reductions in
109 sub-cloud aerosols and CCN budgets ~~via precipitation scavenging processes~~ (Wood, 2006; Zheng et al.,
110 2022b). Quantitative estimates of these effects remain ambiguous and inconclusive, which are subject to
111 multiple factors such as aerosol physicochemical characteristics, cloud morphology, and MBL dynamics
112 and thermodynamics conditions (Sorooshian et al., 2009; Duong et al., 2011; Diamond et al., 2018;
113 Brunke et al., 2022). Thus, more studies on the aforementioned processes regarding MBL aerosols and
114 clouds over different maritime regions are warranted to pursue an in-depth understanding of aerosol-
115 cloud-precipitation interactions (ACPIs).

116 The Eastern North Atlantic (ENA) stands as a desirable region for exploring MBL clouds in the
117 mid-latitude, with Graciosa Island in the Azores (39.09°N, 28.03°W) representing a focal point for
118 ~~studies of ACPIs~~. Located between the mid-latitude and subtropical climate zones, Graciosa ~~Island~~ is
119 subject to the meteorological influence of both the Icelandic Low and the Azores High, and the influence
120 of aerosols ranging from pristine marine air masses to those heavily influenced by continental emissions
121 from North America and Northern Europe (Logan et al., 2014; Wood et al., 2015; Wang et al., 2020).
122 Addressing the need for sustained research into the MBL clouds, the recent Aerosol and Cloud
123 Experiments in the Eastern North Atlantic (ACE-ENA) aircraft campaign (J. Wang et al., 2022) ~~was~~
124 conducted in the summer (June and July) 2017 (ACE-ENA Sum) and winter (January and February)
125 2018 (ACE-ENA Win). During these two intensive operation periods (IOPs) of ACE-ENA, the research
126 aircraft accrued abundant in-situ measurements of aerosols, clouds, and drizzle properties, providing
127 invaluable resources for studying the ACI and ACPI processes. During the summer, the Azores is located
128 at the eastern part of the high-pressure system, while during the winter, the center of the Azores high

Deleted: once

Deleted: also

Deleted: the

Deleted: such

Deleted: were

134 shifts to the eastern Atlantic and is primarily located directly over the Azores (Mechem et al., 2018; J.
135 Wang et al., 2022). Furthermore, both ACE-ENA Sum and ACE-ENA Win IOPs of, featured
136 anomalously strong high-pressure systems, compared to the 20-year climatology, as shown in Figure S1.
137 This meteorological pattern is favorable to the prevailing and persistent stratocumulus clouds observed
138 during ACE-ENA, especially during the winter IOP, where the enhanced large-scale subsidence can lead
139 to stronger and sharper temperature inversions above the stratocumulus-topped MBL (Rémillard and
140 Tselioudis, 2015; Jensen et al., 2021; Marcovecchio et al., 2022). The ACE-ENA Sum is characterized
141 by anomalously low MBL heights and substantial MBL decoupling (Miller et al., 2021; J. Wang et al.,
142 2022). The winter IOP was under the frequent impacts of the mid-latitude systems and prevalently
143 featured precipitation-generated cold pools, where evaporative cooling alters the thermodynamical
144 structure of the MBL, sustains and enhances turbulence mixing, hence contributes to dynamical
145 perturbations that can influence the behavior of the MBL (Terai and Wood, 2013; Zuidema et al., 2017;
146 Jensen et al., 2021; J. Wang et al., 2022; Smalley et al., 2024). In recent years, many observational studies
147 based on ACE-ENA data have focused on the seasonal contrasts of the aerosol distributions and sources
148 (Y. Wang et al., 2021b; Zawadowicz et al., 2021), the cloud and drizzle microphysics vertical
149 distributions (Wu et al., 2020a; Zheng et al., 2022b), and the impacts of MBL conditions on the cloud
150 structure and morphology (Jensen et al., 2021). However, they seldom analyze the comprehensive
151 interactions between aerosol, clouds, and precipitation.

152 Over the Southern Ocean (SO), the Southern Ocean Clouds Radiation Aerosol Transport
153 Experimental Study (SOCRATES) field campaign (McFarquhar et al., 2021) was conducted during the
154 austral summer (January and February 2018), which marks another valuable piece of the MBL cloud
155 research. The SO, being one of the cloudiest regions globally, is predominantly influenced by naturally
156 produced aerosols originating from oceanic sources due to its remoteness, where the anthropogenic and
157 biomass burning aerosols exert minimal influence over the region (McCoy et al., 2021; Sanchez et al.,
158 2021; Twohy et al., 2021; Zhang et al., 2023). The aerosol budget in this region is primarily shaped by

Deleted: summer

Deleted: winter

Deleted: ACE-ENA

Deleted: the

Deleted: for

Deleted: would

Deleted: inversion

Deleted: summer IOP

Deleted: as well as

168 biological aerosols, which nucleate from the oxidation products of dimethyl sulfide (DMS) emissions, as
169 well as by sea spray aerosols. Hence, the SO provides an unparalleled natural laboratory for discerning
170 the influence of these natural aerosol emissions on the MBL clouds under a pre-industrial natural
171 environment. The summertime SO region, particularly near the SOCRATES focus area, is characterized
172 by more frequently closed-cell mesoscale cellular convection structures (Danker et al., 2022; Lang et al.,
173 2022). Furthermore, the MBL clouds over the SO predominantly consist of supercooled liquid water
174 droplets, which coexist with mixed- and ice-phase processes (Y. Wang et al., 2021a; Xi et al., 2022),
175 while the precipitation phases are examined to be primarily dominated by liquid hydrometeors (Tansey
176 et al., 2022; Kang et al., 2024). The in-situ measurements collected from SOCRATES have cultivated
177 ~~many~~ studies on aerosols, clouds, and precipitation over the SO using both in-situ measurements and
178 model simulations (McCoy et al., 2020; Altas et al., 2021; D'Alessandro et al., 2021), and provides an
179 opportunity to study the liquid cloud processes under a colder ~~climate~~. As shown in Figure S1c, ~~our~~
180 ~~composite analysis of the synoptic pattern shows that~~ the SOCRATES cloud cases used in this study are
181 located ahead of the anomalously strong thermal ridge and behind the thermal trough, providing ~~an~~
182 ~~environment~~ favorable to closed cellular MBL cloud structures (McCoy et al., 2017; Lang et al., 2022).
183 ~~Since the~~ region of selected SOCRATES cloud cases crosses a larger latitudinal zone and is under more
184 consistent influence of mid-latitude cyclone systems than the ACE-ENA during the summer IOP, the
185 cloud sampling periods used in this study majority reside in the closed-cell MBL stratocumulus decks.

186 The cloud cases selected from the ACE-ENA and SOCRATES ~~campaigns~~ share similar cloud
187 morphology (stratocumulus) while experiencing different aerosol sources and meteorological conditions.
188 ~~A synergistic approach that compares~~ data from these different field campaigns can provide valuable
189 insights to the community regarding the dominant physical processes of the interactions between aerosols,
190 clouds, and precipitation under the influence of different MBL dynamic and thermodynamic conditions.
191 This study targets the similarities and differences in the MBL aerosol, cloud, and drizzle properties, their
192 distribution and evolution, and more appealingly, the ACIs and ACPIs between the two campaigns. The

Deleted: numerous

Deleted: nature

Deleted: compositely speaking,

Deleted: a set up

Deleted: the

Deleted: The

Deleted: Using a

Deleted: to compare

201 data and methods used in this study are introduced in section 2. The aerosol and CCN properties in the
202 above- and sub-cloud regimes, as well as the vertical distributions of MBL cloud and drizzle properties,
203 are examined in section 3. The ACI, precipitation susceptibility and drizzle impacts on the sub-cloud
204 aerosols and CCN (ACPI) are discussed in section 4. Finally, the results are summarized, and the
205 importance of this study is discussed in section 5.

Deleted: findings

207 2. Data and methods

208 2.1 Cloud and drizzle properties

209 The in-situ measurements of MBL cloud properties are temporally synchronized to 1 Hz
210 resolution, corresponding to approximately 100 m (5 m) of horizontal (vertical) sampling. The sampling
211 locations of the selected cases are indicated by the white dots in Figure S1. The Fast Cloud Droplet Probe
212 (FCDP) onboard the aircraft during ACE-ENA can detect droplets with diameter (D_p) ranging from 1.5
213 μm to 50 μm , with the size bins of the probe between 1 and 3 μm (Glienke and Mei, 2020). SOCRATES
214 used a similar CDP to measure droplets from 2 μm to 50 μm at a 2 μm probe size bin width. Both ACE-
215 ENA and SOCRATES leverage the Two-Dimensional Stereo Particle Imaging Probe (2DS) to discern
216 droplets with diameters from 5 μm to 1280 μm (Lawson et al., 2006; Glienke and Mei, 2019). The 2DS
217 in-situ measurements are used as additional screening to eliminate the ice particles with diameters larger
218 than 200 μm . Moreover, the University of Washington Ice-Liquid Discriminator product, which is a
219 Machine-learning-based single-particle phase classification of the 2DS images (Atlas et al., 2021), is
220 used to identify small ice crystals when available. Through these three datasets, we can tease out the ice-
221 dominated period to the highest extent possible and focus on the liquid cloud processes and ACI during
222 SOCRATES (Wang et al., 2021).

Deleted: While the

Deleted: will be

Deleted: utmost

Deleted: the

223 Although these in-situ measurements can provide “ground-truth” datasets, their uncertainties
224 must be properly analyzed and data quality must be controlled before being applied to scientific studies.
225 The uncertainties of FCDP in sizing and concentration are approximately 30% and 20%, respectively

231 (Baumgardner et al., 2017). Considering the significant uncertainty in the concentration of smaller
 232 particles from a photodiode probe such as 2DS (Baumgardner & Korolev, 1997; Wang et al., 2021), a
 233 diameter of 40 μm is used as the demarcation line between cloud droplets and drizzle drops (Wood et al.,
 234 2005). Then droplet number concentrations in the overlapping size bin between FCDP and 2DS are
 235 redistributed assuming a gamma distribution, thereby a complete size spectrum of cloud and drizzle can
 236 be merged from FCDP and 2DS measurements. Hence, the cloud and drizzle microphysical properties
 237 can be calculated.

238 The cloud droplet number concentration (N_c) is given by:

$$239 \quad N_c = \int_2^{40} n(D_p) dD_p, \quad (1)$$

240 The cloud droplet effective radius (r_c , Hansen and Travis, 1974) is given by:

$$241 \quad r_c = \frac{\int_2^{40} r_p^3 n(D_p) dD_p}{\int_2^{40} r_p^2 n(D_p) dD_p}, \quad (2)$$

242 The cloud liquid water content (LWC_c) can be calculated by:

$$243 \quad LWC_c = \frac{4}{3} \pi \rho_w \int_2^{40} D^3 n(D_p) dD_p, \quad (3)$$

244 where ρ_w is water density.

245 Similarly, the drizzle drop number concentration (N_d) and liquid water content (LWC_d) can be calculated
 246 using the size distribution from 40 μm to 1280 μm . Particularly, the drizzle mean mass diameter (D_{mmd})
 247 is given by:

$$248 \quad D_{mmd} = \left(\frac{\int_{40}^{1280} D_p^3 n(D_p) dD_p}{\int_{40}^{1280} n(D_p) dD_p} \right)^{1/3}, \quad (4)$$

249 This quantity is chosen because the D_{mmd} denotes the diameter of average mass (the third-moment
 250 average) of the drizzle size distribution, which provides the link between the number concentration and
 251 the mass concentration of drizzle droplets in a sample (Hinds, 1999).

252 Adapting the method in Zheng et al. (2022b), the cloud base precipitation rate (R_{CB}) is given by:

$$R_{CB}(mm/hr) = 6\pi * 10^{-4} \int_{40\mu m}^{1280\mu m} D_{p,mm}^3 n(D_{p,mm}) U_{\infty}(D_{p,mm}) dD_{p,mm}, \quad (5)$$

in order to match the unit conversion, the $D_{p,mm}$ is diameter in unit of mm, $n(D_{p,mm})$ is drizzle number concentration in every size bin with a unit of # $m^3 mm^{-1}$, and $U_{\infty}(D_{p,mm})$ is terminal velocity in given size bin, which is calculated from the full Reynolds number theory as in Pruppacher and Klett (2010).

The combined threshold of $N_c > 5 cm^{-3}$ and $LWC_c > 0.01 g m^{-3}$ is used for determining the valid cloud samples and cloud boundaries (Wood, 2005; Zheng et al., 2022b). The complete cloud vertical profiles from sub-cloud to the above-cloud are selected during the ACE-ENA and SOCRATES IOPs, in which the flight strategy includes sawtooth and spiral cloud transects and ramping cloud sampling. The precipitation conditions are determined by whether samples of $N_d > 0.001 cm^{-3}$ exists below the cloud base height. In total, the selected numbers of cloud (precipitating cloud) profiles are 18 (13), 26 (13), and 28 (24) for ACE-ENA Sum and ACE-ENA Win. and SOCRATES, respectively. The detailed selected cloud profiles, with their cloud-base heights (z_t), cloud-top heights (z_b) and cloud thicknesses ($H_c = z_t - z_b$) are listed in Table S1, along with the cloud profile macrophysics.

Furthermore, the assessments of ACI are significantly impacted by the MBL dynamic and thermodynamic conditions. Jones et al. (2011) suggested that the MBL would be in a well-mixed and coupled condition when the difference in liquid water potential temperature (θ_L) and total water mixing ratio (q_t) between the bottom of MBL and the inversion layer are less than 0.5 K and 0.5 $g kg^{-1}$, respectively. The cases selected for this study feature both coupled and decoupled MBL conditions, particularly during ACE-ENA Sum, which is characterized by anomalously low MBL heights and substantial MBL decoupling. Previous studies found that under decoupled conditions, the aerosols, CCN, and moisture sources near the surface are disconnected from the cloud layer aloft, hence exerting a much less effective impact on cloud microphysics (Zheng et al., 2022a; Christensen et al., 2023; Su et al., 2024). Therefore, we adapt and modify the metric in Jones et al. (2011) to calculate the sub-cloud coupled layer, in order to quantify the degree to which aerosols and CCN measured sub-cloud are in a well-mixed state

Deleted: summer
Deleted: winter IOPs along with
Deleted:
Deleted:

Deleted: /

Deleted: summer
Deleted: ,
Deleted: the
Deleted: ,
Deleted: the

287 and can represent the actual interaction (or contact) with the cloud layer. In this study, the q_t and θ_L at
288 the cloud base are calculated, and then their vertical variations are examined starting from the altitude of
289 cloud base (z_b) and looking downward. As such, the coupled point height (z_{cp}) is defined as the altitude
290 where the downward vertical changes in q_t and θ_L exceed 0.5 K and 0.5 g kg^{-1} , respectively. Hence, the
291 coupled layer thickness ($H_{cp} = z_t - z_{cp}$) is defined as the layer between the cloud top height (z_t) and
292 coupled point height (z_{cp}), hence the selection of the aerosols and CCN within the below-cloud part of
293 the coupled layer can be viewed as in contact with the cloud. An example of the coupled layer
294 identification is shown in Figure S2. Therefore, the degree of MBL decoupling (D_{cp}) can be quantified
295 as the ratio of the coupled point height (z_{cp}) to the cloud base height (z_b), where $D_{cp} = z_{cp}/z_b$. As
296 shown in Table S1, the ACE-ENA **Sum** feature with highest degree of decoupling (averaged $D_{cp} = 0.504$),
297 compared to the ACE-ENA **Win** ($D_{cp} = 0.370$) and SOCRATES ($D_{cp} = 0.277$).

Deleted: /

Deleted: summer

Deleted: winter

299 2.2 Aerosol properties

300 The total aerosol number concentrations (N_a) from ACE-ENA and SOCRATES are measured by
301 the airborne Condensation Particle Counter (CPC) models 3772 and 3760A, which **count** the number of
302 aerosols with diameter (D_p) larger than 3 nm and 11 nm, respectively (Kuang and Mei, 2019;
303 SOCRATES Low Rate Data, 2022). Additionally, the Passive Cavity Aerosol Spectrometer (PCASP)
304 onboard the ACE-ENA aircraft is capable of sizing the aerosol with D_p ranging from 0.1 μm to 3.2 μm
305 (Goldberger, 2020). **The** ultra-high sensitivity aerosol spectrometer (UHSAS) measures the size-resolved
306 aerosol distribution from 0.06 μm to 1.0 μm during SOCRATES (Uin, 2016). Therefore, the number
307 concentrations of accumulation mode aerosols (N_{ACC} , 0.1 μm -1 μm) can be discerned from the PCASP
308 and UHSAS aerosol size distributions. **Aitken mode aerosols** (N_{Ait} , $< 0.1 \mu\text{m}$) from **ACE-ENA are**
309 **retrieved** by the fast integrated mobility spectrometer (FIMS), which can size the aerosol down to 9 nm
310 (Olfert et al., 2008), while the N_{Ait} from SOCRATES is limited to 0.06 μm – 0.1 μm due to the limitation

Deleted: counts

Deleted: While the

Deleted: The

Deleted: the

Deleted: is given

319 of UHSAS. As for the CCN measurements, the ACE-ENA utilized the Dual-Column CCN Counter at
320 two constant supersaturation levels of 0.15% and 0.35% (Uin and Mei, 2019), while the CCN number
321 concentration (N_{CCN}) during SOCRATES was measured under various supersaturation levels from 0.06%
322 to 0.87% using a scanning CCN counter (Roberts and Nenes, 2005). In this study, N_{CCN} at 0.35%
323 supersaturation ($N_{CCN0.35\%}$) is used to ensure a direct comparison between ACE-ENA and SOCRATES.
324 The aerosol measurements are in the temporal resolution of 1 Hz. Note that the aerosol and CCN data
325 are quality-controlled by removing the data point where the $N_c + N_d$ greater than 5 cm^{-3} or N_d greater
326 than 0.01 cm^{-3} , to filter out the contamination of the cloud droplets, and drizzle water splashing.

Deleted: 1Hz

327 The sub-cloud aerosols and CCN are selected within the below cloud base part of the coupled
328 layer, which is described in the last section, in order to better assess the aerosol-cloud interactions. The
329 above-cloud aerosols and CCN are selected between the cloud top and 200 m above. Note that the
330 selection criteria of 200 m above the cloud top would inevitably induce uncertainty in the cloud top ACI
331 assessment, depending on the vertical trend of the individual aerosol profile. Over the Southeast Atlantic,
332 Gupta et al. (2021) conducted an analysis focusing particularly on the differing impacts when biomass
333 burning aerosols are in contact with marine stratocumulus cloud tops, using 100 m above as the
334 demarcation, versus when they are separated by various distances, and found that significant differences
335 were observed in cloud microphysics, owing to different droplet evaporation and nucleation, compared
336 to profiles which aerosols and cloud layer are separated. That result is in agreement with the modeling
337 sensitivity study over the Eastern North Atlantic by Wang et al. (2020), who found that aerosol plumes
338 can exert impacts on the cloud-top microphysics only when they are in close contact with the cloud layer.

Deleted: profiles

339 During much of the ACE-ENA campaign, nearly constant (and sometimes decreasing) vertical
340 atmospheric profiles of aerosol concentration were observed within a few hundred meters above the
341 cloud top. Aerosol intrusions due to long-range transport, particularly during the summer season, were
342 observed to induce an elevated aerosol layer in higher altitudes that was not in contact with the cloud
343 layer. The frequent new particle formation events during SOCRATES significantly alter the free-

Deleted: In most cases,

Deleted: feature is a rather stable or slightly

Deleted: profile

Deleted: , while the

Deleted: transports

Deleted: summertime, will

Deleted: is

Deleted: will

354 troposphere Aitken mode aerosol budget, ~~but the aerosols~~ would need to further subside to impact the
355 cloud (McCoy et al., 2021; Zhang et al., 2023). ~~Note that from previous studies on ACE-ENA and~~
356 ~~SOCRATES, the aerosol vertical profiles within ~200 m above the cloud layers are typically found to~~
357 ~~have less variation (Wang et al., 2020; Wang et al., 2021; McCoy et al., 2021; Zhang et al., 2023), hence~~
358 ~~representing the aerosol layers in contact with the cloud. Hence,~~ the 200 m criterion used in this study
359 ~~provides a sufficient~~ sample size ~~population~~ for statistical analysis.

Deleted: they

Deleted: Therefore

Deleted: captures the close-to-cloud aerosol plumes and

Deleted: enough

361 3. Aerosol, cloud, and drizzle properties of selected cases

362 3.1 Aerosols and CCN in above- and sub-cloud regimes

363 The probability density functions (PDFs) of aerosols, CCN, and cloud microphysical properties
364 from selected cases during the ACE-ENA and SOCRATES field campaigns are presented in Figure 1.
365 Notably, the N_a , N_{Acc} and $N_{CCN0.35\%}$ values from the SOCRATES are the highest among the three IOPs,
366 followed by the ACE-ENA ~~Sum~~ and ~~ACE-ENA Win~~ as illustrated in both above-cloud (Figs. 1a-1c) and
367 sub-cloud regimes (Figs. 1d-1f). Such variations can be linked to the different aerosol sources in the
368 ACE-ENA and SOCRATES regions, especially during the summer and winter seasons over the Azores.

Deleted: summer

Deleted: winter

369 In the SOCRATES region, according to the previous studies involving back-trajectory analyses,
370 dominant air masses within the MBL primarily originate from the south or from the west, skirting the
371 Antarctic coast (Zhang et al., 2023), while the air masses above the MBL follow a similar transport
372 pathway, they can also originate from the tip of southern Africa and be transported southeast along the
373 warm conveyor belt (McCoy et al., 2021). ~~Above-cloud aerosol $N_{CCN0.35\%}$ values analyzed during~~
374 ~~SOCRATES~~ (674.6 cm^{-3}) are primarily constituted by the Aitken mode aerosols because the mean N_{Acc}
375 is only 62.5 cm^{-3} . Previously, McCoy et al. (2021) reported average $N_{CCN0.35\%}$ values of 680.69 cm^{-3} ,
376 546.28 cm^{-3} and 465.05 cm^{-3} for mid-troposphere, above and below cloud for the multiple SOCRATES
377 cases, respectively. For individual cases, the above cloud aerosols vary from a couple hundred to over a

Deleted: The SOCRATES above-cloud aerosols

385 thousand particles per cubic centimeter (McCoy et al., 2021; Zhang et al., 2023). These aerosols are
386 predominantly produced from the oxidation of biogenic gases, notably dimethyl sulfide (DMS) emitted
387 by marine biological productivity (Sanchez et al., 2018; McCoy et al., 2020). The rising air currents in
388 MBL transport these particles into the free troposphere with dominant aerosol population over the SO
389 (McCoy et al., 2021; Sanchez et al., 2021). Hence, it reinforces the notion that the SO represents a pre-
390 industrial marine environment where the influence of anthropogenic and biomass-burning aerosols is
391 mostly negligible (McCoy et al., 2020, 2021).

392 Conversely, the ENA region experiences aerosols of varied origins, spanning maritime air masses
393 to those heavily influenced by continental emissions from North America or Northern Europe, especially
394 during the summer season (Logan et al., 2014; Wang et al., 2020). The summer air mass back-trajectories
395 within the MBL strongly feature recirculating flow around the Azores high. During the wintertime,
396 however, the air masses predominantly originate in the FT, are transported above the MBL, and are then
397 further entrained to the MBL by large-scale subsidence, indicating less influence from continental
398 pollution (Y. Wang et al., 2021b). During the ACE-ENA Sum, the MBL is enriched by sulfate and
399 carbonaceous particles (Y. Wang et al., 2021b; Zawadowicz et al., 2021). This enhancement is attributed
400 both to local generation from DMS and to the long-range transport from the continental air masses,
401 resulting in the mean N_a of 312.6 cm^{-3} and 301.5 cm^{-3} for above- and sub-cloud regimes, respectively.
402 The ACE-ENA Win exhibits the lowest aerosol and CCN concentrations, predominantly sourced from
403 local maritime influences, and coupled with reduced continental air mass intrusions (Zheng et al., 2018;
404 Y. Wang et al., 2021b).

405 Figure 1a and 1d reveals that there are more above-cloud N_a during the three IOPs than sub-cloud
406 values, especially during the SOCRATES. The higher above-cloud N_a values from the three IOPs are
407 primarily contributed by Aitken mode aerosols because their corresponding N_{Acc} values are much lower
408 (Figs. 1a & 1b). It is interesting to note that the above-cloud $N_{CCN0.35\%}$ values exceed the N_{Acc} for all
409 three IOPs (Figs. 1b & 1c), implying that a significant fraction of Aitken mode aerosols can be activated

Deleted: the

Deleted: (FT)

Deleted: summertime

Deleted: summertime

Deleted: down

Deleted: summer

Deleted: campaign

Deleted: winter

Deleted: &b

Deleted: &c

420 to become CCN, corroborating findings from earlier studies (McCoy et al., 2021; Zheng et al., 2021).
421 For the sub-cloud regime, the N_a values ~~for~~ SOCRATES and ACE-ENA ~~Win~~ are ~70-80% of their
422 corresponding above-cloud values, and the N_a during ACE-ENA ~~Sum~~ is almost identical to its above-
423 cloud value. Notice that the sub-cloud N_{Acc} values from ~~the~~ three IOPs are more than double the above-
424 cloud N_{Acc} values, and most of the sub-cloud accumulation mode aerosol can be activated to become
425 CCN at SS of 0.35%. It is interesting to note that the higher $N_{CCN0.35\%}$ at ~~the~~ sub-cloud layer during
426 SOCRATES may partially ~~be a result of~~ aerosols ~~being positively impacted by cloud dynamic processes~~
427 (Figs. 1e, ~~& 1f~~), which is suggested by previous studies (McCoy et al., 2021; Zhang et al., 2023) and will
428 be further discussed in ~~the following paragraphs~~.

Deleted: during

Deleted: winter

Deleted: summer

Deleted: from the cloud process on

Deleted: &f

Deleted: Section 3.1

429 To further investigate the above- and sub-cloud aerosol properties from ~~the~~ three IOPs, the aerosol
430 droplet size distributions are analyzed in Figure 2. It is evident that SOCRATES aerosols have the highest
431 concentrations of Aitken mode particles ($D_p = 0.06 - 0.1 \mu\text{m}$, given that the $< 0.06 \mu\text{m}$ is not available
432 from UHSAS) for ~~the~~ above- and sub-cloud regimes. McCoy et al. (2021) and Zheng et al. (2021)
433 identified analogous origins and formations of the above-cloud Aitken mode aerosols over ~~the~~ SO and
434 ENA regions and concluded that these aerosols primarily originate from the nucleation of photo-
435 oxidation products of DMS, notably H_2SO_4 and MSA, in the free troposphere. ~~The~~ differential
436 concentrations can be ascribed to the fact that sea-surface DMS concentrations in the SO are generally
437 higher than those in the ENA region (Aumont et al., 2002; Zhang et al., 2023). Moreover, DMS emissions
438 in the ENA during ~~the~~ summer ~~season~~ surpass those during winter (Zawadowicz et al., 2021). For the
439 accumulation mode aerosols ($0.1 - 1 \mu\text{m}$), the N_{Acc} values for both above- and sub-cloud regimes during
440 SOCRATES decrease monotonically with particle size. The results in Figure 2 further support the finding
441 that Aitken mode aerosols are dominant over the SO. The N_{Acc} values during ACE-ENA show slight
442 uplifts for the small accumulation mode aerosols ($< 0.3 \mu\text{m}$), particularly ~~during the~~ summer, reflecting
443 the signal of potential long-range transport of fine-mode aerosols (Wang et al., 2020; Y. Wang et al.,

Deleted: both

Deleted: both

Deleted: (FT).

Deleted: for

2021b). Consequently, such comparison reinforces the notion that the SO represents a largely pre-industrial marine environment, wherein the influence of anthropogenic and biomass-burning aerosols is minimal (McCoy et al., 2020, 2021; Zhang et al., 2023).

When contrasting the aerosol size distributions in the sub-cloud regime (Fig. 2b) with those in the above-cloud regime, the influence of cloud processing on aerosols is discernibly non-trivial, particularly under the cloud-topped MBL conditions examined in this study. The FT aerosols can be entrained, and contribute to the population of Aitken mode aerosols within the MBL, and the sub-cloud aerosols can also be subject to the influence of new particle formation in the upper MBL, though arguably less effective than those within the FT (Zheng et al., 2021). Additionally, in-cloud Brownian capture can lead to a substantial reduction in Aitken mode aerosols (Hudson et al., 2015; Wyant et al., 2022), providing the rationale for the observed decrease in Aitken mode aerosols from above- to the sub-cloud regime, especially for particles smaller than 0.07 μm . In addition, cloud chemical processing, such as the aqueous-phase condensation of sulfuric acid onto the aerosol cores inside the cloud droplets, is particularly pronounced during the transitioning of Aitken mode aerosols to accumulation mode aerosols (Hudson et al., 2015; Zhang et al., 2023).

The larger Aitken mode aerosols ($> 0.07 \mu\text{m}$) in the above- and sub-cloud regimes can effectively grow to accumulation mode aerosols through coagulation and water vapor diffusional growth (Covert et al., 1996), contributing to the elevated accumulation mode aerosol distribution and increased N_{Acc} in the sub-cloud regime. These processes are evident by the decrease of critical supersaturations from above-cloud (between 0.35% - 0.4%) to sub-cloud (between 0.3% - 0.35%) during SOCRATES (Fig. S3) because the aerosol droplet sizes are enlarged and more readily become CCN. Furthermore, the collision-coalescence combines mixtures of large and small cloud droplets, and results in the sub-cloud aerosol residuals shifting towards the larger size upon the drizzle droplet evaporation below the cloud. This partially elucidates the observed increase in the tail-end of the accumulation mode aerosol distribution for all three IOPs. The elevation in sub-cloud coarse mode aerosols observed for both ACE-ENA IOPs

Deleted: down

Deleted: From both above- to sub-cloud regimes, the

Deleted: be

Deleted: enlarged

Deleted: evidenced

484 (as seen in Fig. 2) can be attributed to the evaporation of collision-coalescence-enlarged ~~drizzle droplets~~
485 and the intrusion of sea spray aerosols (e.g., sea salt), as illustrated and analyzed based on a summertime
486 case study that exhibits the signal of cloud-processing aerosols (Zheng et al., 2022b), and the long-term
487 aerosol physicochemical properties over the ARM-ENA ground-based observatory (Zheng et al., 2018)
488 particularly during the winter season where the production of sea spray aerosol is prevalent.

Deleted: drizzles

490 3.2 ~~Distribution of bulk cloud microphysical properties,~~

Deleted: Bulk

Deleted: distribution

491 The PDFs of MBL cloud microphysical properties (N_c , r_c , LWC_c) derived from aircraft in-situ
492 measurements from the three IOPs are shown in Figures 1g-1i. The mean microphysical properties for
493 the individual cloud profiles are listed in Table S2. ~~The~~ SOCRATES has the highest sub-cloud aerosols
494 and CCN, and subsequently feature a larger number of smaller cloud droplets, given the highest N_c
495 (148.3 cm^{-3}) and smallest r_c ($8 \text{ }\mu\text{m}$) among the three IOPs. These results have further confirmed and
496 reassured our understanding of the aerosol first indirect effect: ~~a larger population of~~ aerosols induce ~~a~~
497 ~~higher number concentration of small~~ cloud droplets under constrained liquid water content conditions,
498 ~~and~~ thus the MBL clouds reflect more incoming solar radiation (Twomey, 1977). The ACE-ENA ~~Win~~
499 clouds feature the fewest N_c (70.6 cm^{-3}) and largest r_c ($9.8 \text{ }\mu\text{m}$), while the N_c and r_c (89.4 cm^{-3} and $9 \text{ }\mu\text{m}$)
500 during ACE-ENA ~~Sum~~ fall between the SOCRATES and ACE-ENA ~~Win~~ values. Considering the
501 aerosol competing effect against the available water vapor, the relatively abundant aerosols in
502 SOCRATES might account for the ~~observed~~ narrower r_c distribution, which peaks between $6 - 10 \text{ }\mu\text{m}$.
503 SOCRATES has a lower cloud-layer water vapor mixing ratio (figure not shown) compared to ACE-
504 ENA because the SO region has been observed to contain less precipitable water vapor than the ENA
505 region due to the colder sea surface temperatures (Marcovecchio et al., 2023). Therefore, the aerosol and
506 cloud properties in Figure 1 promise further examination of different cloud microphysical responses to
507 aerosols via the ACI process. Note that the $N_{CCN0.35\%}$ ~~are~~ lower than N_c values during the ACE-ENA

Deleted: The results in Figure 1 have demonstrated that aerosol/CCN sources and concentrations, especially from the sub-cloud regime, play an important role in cloud droplet formation and evolution. For example, the

Deleted: more

Deleted: more and smaller

Deleted: (higher N_c and smaller r_c)

Deleted: wintertime

Deleted: summer

Deleted: winter

Deleted: and N_c values

522 ~~Win~~, which is also confirmed in previous studies (J. Wang et al., 2022; Wang et al., 2023). This
523 interesting phenomenon can potentially be attributed to a combination of factors, including lower MBL
524 aerosol sources, stronger in-cloud coalescence-scavenging depletion of sub-cloud aerosols, and the
525 aircraft snapshots capturing the equilibrium states of aerosols and cloud due to enhanced aerosol
526 activations induced by stronger updrafts during the ACE-ENA ~~Win~~ (J. Wang et al., 2022). This thereby
527 compels further investigation into the potential impacts of precipitation on the MBL CCN budget, ~~which~~
528 ~~is further~~ discussed in Section 4.

Deleted: winter IOP

Deleted: winter

Deleted: . These aerosol-cloud-precipitation interactions (ACPIs) will be

530 3.3 Vertical distributions of cloud and drizzle microphysics

531 The vertical distributions of the cloud and drizzle microphysical properties within the cloud layer
532 from the three IOPs are shown in Figure 3. To ensure the representativeness of the vertical profiles, all
533 the in-cloud samples are vertically smoothed using a triangular moving average method, and are inverse-
534 distance weighted in every 50 m moving altitude windows. Furthermore, the altitude is then normalized
535 by $z_i = \frac{z - z_{base}}{z_{top} - z_{base}}$, where $z_i = 0$ denotes cloud base and $z_i = 1$ denotes cloud top. Consistent with
536 previous discussions on the bulk microphysics distribution, the mean N_c values from SOCRATES are
537 consistently higher than ACE-ENA ~~Sum~~, and ~~ACE-ENA Win~~ for the entire cloud layer, with a slight
538 increase ranging from the cloud base to the upper-middle part ($z_i \approx 0.85$) and then decreasing toward
539 the cloud top (Fig. 3a). All r_c values from the three IOPs show a near-linear increase from cloud base to
540 top, with the smallest values observed during SOCRATES and the largest values observed during ACE-
541 ENA ~~Win~~ (Fig. 3b).

Deleted:

Deleted: summer

Deleted: winter

Deleted: due to cloud-top entrainment

Deleted: winter

542 The warmer and drier air near the cloud top entrains into the cloud layer and further mixes
543 downward, often resulting in the evaporation of small cloud droplets and the shrinking of droplet sizes,
544 which oppose condensational growth (Desai et al., 2021). Decreases in both N_c and LWC_c , and the
545 reduced growth of r_c near the cloud top ($z_i > 0.85$) support signals of cloud-top entrainment mixing

555 during all three IOPs. It is interesting to note that the r_c values from SOCRATES increase monotonically
556 from cloud base to top, while the r_c values from both ACE-ENA Sum, and ACE-ENA Win increase until
557 $z_i \approx 0.8$ and then remain nearly constant, although all of their N_c values (at $z_i \approx 0.8$) decrease towards
558 the cloud top. When dry air entrainment occurs at the cloud top, some of the upper-level smaller cloud
559 droplets will evaporate, which leads to decreases in N_c (Fig. 3a). As a result, the nearly constant r_c values
560 (at $z_i > 0.8$) might represent the equilibrium balance between two competing processes: cloud droplet
561 condensational and collision-coalescence growths, and the entrainment mixing evaporation effects.

562 Carrying the distinct discrepancies in the mean values for all layers, the N_c and r_c from ACE-
563 ENA Sum, and ACE-ENA Win clouds experienced similar vertical evolutions as SOCRATES. The
564 increases of r_c (Δr_c) from cloud base to cloud top are $4.03 \mu\text{m}$, $4.78 \mu\text{m}$ and $5.85 \mu\text{m}$, with percentage
565 increases of 66%, 68% and 79%, for SOCRATES, ACE-ENA Sum, and ACE-ENA Win, respectively.

566 Even though, theoretically, the condensational growth effect would be more pronounced on smaller cloud
567 droplets due to their smaller surface area (Wallace and Hobbs, 2006), SOCRATES exhibits the thickest
568 mean cloud thickness but experienced the least r_c increase among the three IOPs. This suggests that high
569 aerosol loading limits the overall growth of the cloud droplet size distribution (DSD) in SOCRATES
570 clouds, while the ACE-ENA Win clouds show the strongest r_c increase, in contrast. This comparison
571 indicates different cloud microphysical responses to aerosol perturbations in the three IOPs, which will
572 be further discussed in Section 4.1. The LWC_c values from the three IOPs are comparable to each other.

573 The vertical distributions of MBL cloud microphysical properties examined in this study are in good
574 agreement with the previous studies conducted on these two field campaigns (Wu et al., 2020a; Y. Wang
575 et al., 2021a; J. Wang et al., 2021; Wang et al., 2023). Cloud adiabaticity is a key parameter as it provides
576 insight into the degree of mixing and microphysical processes occurring within clouds. The sub-adiabatic
577 conditions indicate that the LWC_c is less than what would be expected in an adiabatic scenario, often due
578 to processes such as in-cloud collision-coalescence and entrainment mixing (Hill et al., 2009; Braun et

Deleted: summer

Deleted: winter

Deleted: As cloud-top entrainment mixing can shrink large cloud droplets via evaporation, depending on the entrainment mixing rate...

Deleted: ,

Deleted: While carrying

Deleted: summer

Deleted: winter

Deleted: the

Deleted: summer

Deleted: winter

Deleted: loadings are limiting

Deleted: winter

Moved (insertion) [1]

593 [al., 2018; Gao et al., 2020; Wu et al., 2020b](#)). In addition, the cloud adiabaticity is defined as $f_{ad} =$
594 LWC_c/LWC_{ad} , where the LWC_{ad} denotes adiabatic LWC (Wu et al., 2020b). As shown in Figure S4,
595 the clouds from all three IOPs feature certain levels of sub-adiabaticity above the cloud base. Considering
596 the inter-cloud layer-mean f_{ad} , the campaign-mean f_{ad} values are 0.689 ± 0.229 , 0.542 ± 0.143 , and
597 0.490 ± 0.207 for SOCRATES, ACE-ENA ~~Sum~~, and ~~ACE-ENA Win~~, respectively.

598 To quantitatively evaluate the impact of cloud-top entrainment mixing rate on cloud droplets, we
599 adapt the method of Albrecht et al. (2016), where the cloud-top entrainment rate (w_e) can be expressed
600 as

$$601 \quad w_e = A_\sigma * \sigma_w / R_{i\sigma} , \quad (6)$$

602 where the turbulence kinetic energy (TKE) dissipation coefficient A_σ is empirically taken as 26 as in
603 Albrecht et al. (2016), and the $R_{i\sigma}$ is the buoyancy Richardson number calculated by $(g/\theta_0) *$
604 $(\Delta\theta_v h / \sigma_w^2)$. σ_w denotes the standard deviation of vertical velocities taken near the cloud top ($z_i > 0.9$),
605 and h is the MBL height. θ_0 is the reference potential temperature and $\Delta\theta_v$ is the virtual potential
606 temperature difference across the temperature inversion layer above the cloud. Given the valid cloud-top
607 virtual potential temperature and vertical velocity measurements for the selected cloud cases, the
608 averaged w_e values are $0.570 \pm 0.834 \text{ cm s}^{-1}$, $0.581 \pm 0.560 \text{ cm s}^{-1}$, and $0.960 \pm 1.127 \text{ cm s}^{-1}$ for SOCRATES,

609 ACE-ENA ~~Sum~~, and ~~ACE-ENA Win~~, respectively. The stronger w_e during ACE-ENA ~~Win~~ might be
610 induced by the generally weaker cloud-top inversions and stronger near-cloud top turbulence, (Fig. 5a),
611 compared to the summertime when the ENA is dominated by the large-scale high-pressure system (Ghate

612 et al., ~~2021~~). ~~Within the above-cloud inversion layer, the temperature (water vapor mixing ratio)~~
613 ~~differences ΔT (Δq) are 1.76 K (-1.75 g kg⁻¹), 1.54 K (-1.66 g kg⁻¹) and 1.48 K (-1.09 g kg⁻¹) for~~
614 ~~SOCRATES, ACE-ENA Sum, and ACE-ENA Win, respectively. The virtual potential temperature~~
615 ~~differences $\Delta\theta_v$ are 4.90 K, 5.16 K, and 3.82 K, for SOCRATES, ACE-ENA Sum, and ACE-ENA Win,~~
616 ~~respectively, indicating relatively dryer entrained airmasses during SOCRATES and ACE-ENA Sum.~~

Moved up [1]: Hill et al., 2009; Braun et al., 2018; Gao et al., 2020; Wu et al., 2020b).

Deleted: summer and winter, respectively. It is well known that cloud sub-adiabaticity is primarily induced by the in-cloud collision-coalescence and the entrainment mixing processes (...)

Deleted:

Deleted: summer

Deleted: winter

Deleted: winter

Deleted: ,

Deleted: 2021).

629 Considering the near cloud-top proportion of cloud where the LWC_c experienced decrease, the difference
 630 in LWC_c (between the cloud-top value and the upper-middle cloud maximum for the mean profiles) for
 631 the ACE-ENA Sum (-0.032 g m^{-3}) is higher than the reductions in winter (-0.018 g m^{-3}) and SOCRATES
 632 (-0.009 g m^{-3}), albeit that the w_e for ACE-ENA Sum is comparable to SOCRATES, and much lower than
 633 ACE-ENA Win values. The warmer and dryer entrained air can partially contribute to the greater LWC_c
 634 reduction and the lower f_{ad} (0.39) during the ACE-ENA Sum than those during the ACE-ENA Win
 635 ($f_{ad} = 0.45$) and SOCRATES ($f_{ad} = 0.66$) near the cloud top (Fig. S4). For the three IOPs, the N_c and
 636 LWC_c exhibit stable trends from the cloud base, followed by noticeable decreases near the cloud top
 637 mixing zone, while the changes in r_c trends near the cloud top were not as dramatic as the others. Such
 638 characteristics of the cloud microphysics vertical profiles indicate the signal of inhomogeneous mixing,
 639 which occurs when dry and warm air mixes unevenly and slowly with the cloud air, hence partially
 640 evaporating the cloud droplets (Lehmann et al., 2009; Lu et al., 2011). The results are consistent with
 641 previous research results regarding stratocumulus clouds over multiple field campaigns (Brenquier et al.,
 642 2011; Jia et al., 2019) and with the findings for selected cases during ACE-ENA (Yeom et al., 2021) and
 643 SOCRATES (Sanchez et al., 2020). The near-cloud top r_c profiles ($z_i > 0.8$) for the ACE-ENA cases
 644 exhibit fewer increases compared to SOCRATES, which could be possibly attributed to more effective
 645 mixing due to the stronger entrainment rate, particularly during ACE-ENA Win, eventually reaching a
 646 smaller equilibrium in terms of mean sizes.

647 Figures 3d-3f illustrate the normalized profiles of MBL drizzle microphysical properties. The N_d
 648 values from the three IOPs mimic each other, which all maximize at the cloud top and then monotonically
 649 decrease toward the cloud base (Fig. 3d), while their LWC_d values follow a similar trend, albeit with
 650 relatively large differences (Fig. 3f). In contrast to the N_d and LWC_d trends, the D_{mmd} gradually increase
 651 from cloud top to cloud base (Fig. 3e), making physical sense since the drizzle droplets are typically
 652 formed near the cloud top and continuously grow via collision-coalescence process while falling. The

Deleted:

Deleted: summer

Deleted: summer

Deleted: winter

Deleted: Within the above-cloud inversion layer, the temperature (water vapor mixing ratio) differences ΔT (Δq) are 1.76 K (-1.75 g kg^{-1}), 1.54 K (-1.66 g kg^{-1}) and 1.48 K (-1.09 g kg^{-1}) for SOCRATES, ACE-ENA summer and winter, respectively. Therefore, the

Deleted: summer

Deleted: winter

Deleted: exhibited

Deleted: findings in

Deleted: the

Deleted: the

Deleted: the

Deleted: the

Deleted: winter

671 ACE-ENA Win drizzle D_{mmd} and LWC_d values are distinctively larger than those in ACE-ENA Sum
672 and SOCRATES. It is interesting to note that near the cloud top ($z_i > 0.9$), ACE-ENA Win has
673 comparable N_d but much larger D_{mmd} than the other two IOPs, suggesting that there were more large
674 drizzle embryos formed from large cloud droplets (Fig. 3b) during ACE-ENA Win. It is noteworthy that
675 the D_{mmd} in the lower-half region of the ACE-ENA Win clouds experienced rapid growth from $\sim 80 \mu\text{m}$
676 to $\sim 105 \mu\text{m}$ (Fig. 3e), and this increment of $\sim 25 \mu\text{m}$ contributed to most of the D_{mmd} growth from cloud
677 top to cloud base ($33.5 \mu\text{m}$), indicating a stronger warm-rain process during the winter.

678 In order to further analyze the cloud-to-drizzle conversion processes, the cloud and drizzle DSDs
679 are categorized into four segments based on their relative position within the cloud layer (Fig. 4): upper
680 cloud ($z_i > 0.8$, Fig. 4a), upper-middle cloud ($0.5 \leq z_i < 0.8$, Fig. 4b), lower-middle cloud ($0.2 \leq z_i <$
681 0.5 , Fig. 4c) and lower cloud ($z_i < 0.2$, Fig. 4d). The cloud DSDs ($D_p < 40 \mu\text{m}$) from the three IOPs
682 gradually shift towards larger sizes, moving from the lower to the upper cloud regions. This is
683 accompanied by the narrowing of the cloud DSD ranges, as evidenced by the decline in the relative
684 dispersion of cloud droplets (ϵ), which is defined as the ratio between the standard deviation and the
685 mean radius of the distribution. At the lower portion of the cloud (Fig. 4d), the relatively greater value
686 of ϵ represents the co-existence of the newly formed small cloud droplets from recently activated CCN
687 and the sedimentation of larger droplets from the upper sections of the cloud. In addition, the
688 discrepancies in ϵ between the three IOPs may be attributed to the sub-cloud aerosol differences, which
689 essentially resided in different microphysical regimes. Y. Wang et al. (2021a) stated that higher aerosol
690 loading would lead to increased ϵ due to the water vapor competition effect, supporting the discrepancy
691 between SOCRATES and ACE-ENA Sum, which can be categorized as a water vapor-limited regime.
692 Meanwhile, the ACE-ENA Win exhibits characteristics of an aerosol-limited regime, in which the cloud
693 DSDs tend to be narrower than in the water-limited regime, due to enhanced droplet growth, and the ϵ
694 values further decrease with height via the condensational narrowing effect (J. Chen et al., 2018).

Deleted: wintertime

Deleted: summertime

Deleted: the

Deleted: winter

Deleted: winter

Deleted: winter

Deleted: droplet size distributions (DSD)

Deleted: CCNs

Deleted: summer IOPs

Deleted: -

Deleted: wintertime IOP

706 Notably, ~~for the four cloud portions from cloud base to cloud top, the skewness of summer (winter)~~
707 ~~cloud DSDs are 0.627 (0.271), 0.358 (0.175), 0.098 (-0.063), and -0.362 (-0.554), respectively.~~ The cloud
708 DSDs during ACE-ENA ~~Win~~ exhibit a more pronounced negative skew (to the left) than those during
709 ACE-ENA ~~Sum~~, which can be partially attributed to the activation of more sub-cloud coarse mode
710 aerosols becoming larger cloud embryos, as demonstrated in Fig. 2. These coarse mode aerosols, whether
711 from primary production of sea spray or the residuals of evaporated drizzle drops, are more easily
712 activated (or re-activated) into larger cloud droplets when they intrude (or recirculate) into the cloud
713 layer (Hudson and Noble, 2020; Hoffmann and Feingold, 2023). Nevertheless, it is challenging to
714 pinpoint the actual origins of coarse mode aerosols from the perspective of aircraft observational
715 snapshots, thus requiring further numerical modeling work. ~~Ascending within the cloud, the process of~~
716 water vapor condensation perpetually pushes the DSD towards larger sizes, culminating in a more
717 negatively skewed DSD. Concurrently, the cloud-top entrainment mixing plays a pivotal role in
718 minimizing ϵ in the upper cloud region, as elaborated by Lu et al. (2023).

719 ~~In~~ the upper region of the cloud (Fig. 4a), the ACE-ENA ~~Win~~ clouds contain more cloud droplets
720 close to $40 \mu\text{m}$, albeit the mean N_c is lower. This scenario is conducive to the formation of larger drizzle
721 embryos compared to summertime clouds, as depicted in Fig. 3e. In comparison, the SOCRATES clouds
722 feature a pronounced log-normal DSD than ~~during~~ ACE-ENA, as the DSDs peak at $D_p \sim 15 \mu\text{m}$
723 throughout the cloud, and subsequently, the lack of larger cloud droplets resulted in the smaller drizzle
724 embryos near the cloud top. As the newly formed drizzle drops descend and continuously grow through
725 the collision-coalescence process, the drizzle DSDs ($D_p > 40 \mu\text{m}$) are noticeably broadened. From upper
726 to lower cloud regions, the longer tails of the drizzle DSDs expand at the cost of smaller drizzle drops
727 and cloud droplets via the collision-coalescence process. The clouds observed during ACE-ENA,
728 especially in wintertime, contain more large drizzle drops ($D_p > 200 \mu\text{m}$) than SOCRATES, which is
729 reflected in the distinct differences in the vertical D_{mod} as shown in Fig. 3e.

Deleted: winter

Deleted: summer

Deleted: For the four cloud portions from cloud base to cloud top, the skewness of summertime (wintertime) cloud DSDs are 0.627 (0.271), 0.358 (0.175), 0.098 (-0.063), and -0.362 (-0.554), respectively.

Deleted: Note that in

Deleted: winter

Deleted: the

739 It has been intensively studied that in-cloud turbulence can stimulate collision-coalescence and
740 consequently enhance the drizzle evolution processes (Pinsky et al., 2007; Grabowski and Wang, 2013;
741 Wu et al., 2017; S. Chen et al., 2018). The turbulence strength is characterized by the turbulence kinetic
742 energy (TKE), which is calculated as:

$$743 \quad TKE = \frac{1}{2} (\overline{u'^2} + \overline{v'^2} + \overline{w'^2}), \quad (7)$$

744 where the turbulent perturbations of vertical ($\overline{w'^2}$) and horizontal ($\overline{u'^2}$ and $\overline{v'^2}$) components are
745 calculated as the simple moving variance in a 10 s window centered at the measurement time, without
746 window weighting function, using 1 Hz data for all three IOPs. The w data is confined to an absolute
747 aircraft roll angle of less than 5° (Cooper et al., 2016). Given the average aircraft ground speed of ~ 140
748 m s^{-1} and vertical speed of $\sim 5 \text{ m s}^{-1}$ (Atlas et al., 2020), the smallest resolved wavelength is 140 m. Hence,
749 within the 10s moving window, the $\sim 50 \text{ m}$ in the integral vertical range is able to resolve the eddies up
750 to $\sim 1400 \text{ m}$ in size, and preserve the potential of capturing the inertial subrange.

751 As shown in Figure 5, the vertical wind variances (Fig. 5b) in ACE-ENA Win (layer-mean of
752 $0.244 \text{ m}^2 \text{ s}^{-2}$) are generally higher than those in ACE-ENA Sum ($0.153 \text{ m}^2 \text{ s}^{-2}$) and SOCRATES (0.147
753 $\text{m}^2 \text{ s}^{-2}$), while the horizontal wind variances (Figs. 5c & 5d) are comparable between ACE-ENA Sum
754 and ACE-ENA Win but much higher than the SOCRATES, resulting in higher TKE during ACE-ENA.
755 Note that the higher w'^2 near cloud top corresponds to the stronger entrainment rate in ACE-ENA Win.
756 Near the cloud top, turbulence effectively enhances coalescence between the larger cloud droplets,
757 primarily by increasing the relative velocities between droplets (Magaritz-Ronen et al., 2016; Ghate and
758 Cadeddu, 2019), and this is especially true for the vertical component w'^2 of TKE. The horizontal
759 turbulence components, the u'^2 and v'^2 can also play a role in mixing the ambient air masses and
760 contribute to the broadening of DSD (Wu et al., 2017). The use of TKE provides an illustration that in-
761 cloud turbulence during ACE-ENA is stronger than that observed during SOCRATES. That being said,
762 the quantitative evaluation of the turbulent enhancement of collision-coalescence requires access to the

Deleted: 10s

Deleted: 1Hz

Deleted: /

Deleted: /

Deleted: winter

Deleted: summer

Deleted: Fig

Deleted: d

Deleted: winter

Deleted: summer

Deleted: wintertime

Deleted: While the

Deleted: might be slightly

776 eddy dissipation rate, as typically used in model parameterizations (Grabowski and Wang, 2013; Witte
777 et al., 2019). The smallest scales resolvable with the 1 Hz measurement used in this study are on the
778 order of 140 meters, thus capturing only the larger-scale end of the inertial subrange and larger turbulent
779 motions. Consequently, the ability to resolve smaller eddies and turbulent structures, crucial for
780 understanding the energy cascade within the inertial subrange, is limited by coarse spatial and temporal
781 resolutions and aliasing issues (Siebert et al., 2010; Muñoz-Esparza et al., 2018; Kim et al., 2022).
782 Therefore, to fully resolve the spectrum of turbulence and quantitatively examine energy dissipation and
783 mixing processes, access to higher-frequency measurements is required to capture smaller eddies within
784 the inertial subrange (Siebert et al., 2010; Lu et al., 2011; Waclawczyk et al., 2017). Additionally, further
785 quantifying the entrainment-mixing mechanisms also requires high-frequency eddy dissipation and
786 accurate examination of the mixing time scale (Lehmann et al., 2009; Lu et al., 2011) for individual
787 profiles. Though currently beyond the scope of this study, utilizing the high-rate measurements of
788 velocities available from SOCRATES (at 25 Hz) and ACE-ENA (at 20 Hz) to explore those mechanisms
789 further will be of interest to future investigations.

790 Drizzle formation and evolution in the ACE-ENA Win clouds are noticeably stronger than in the
791 other two IOPs, which could be attributed to multiple factors. First, the ambient aerosols and CCN during
792 winter are substantially fewer, featuring clean environments that promote the formation of generally
793 larger cloud droplets due to the availability of more water content per droplet. Larger cloud droplets are
794 more likely to collide and coalesce into drizzle drops, leading to relatively heavier precipitation (Chen et
795 al., 2011; Duong et al., 2011; Mann et al., 2014). Furthermore, deeper cloud layers with mean thickness
796 of (392.4 m) during ACE-ENA Win were observed when compared to the ACE-ENA Sum clouds (336.3
797 m). In a thicker cloud layer with sufficient turbulence, the residence times of large cloud droplets and
798 drizzle drops would become longer, and the chance of collision-coalescence growth could be effectively
799 increased by recirculating the drizzle drops (Brost et al., 1982; Feingold et al., 1996; Magaritz et al.,
800 2009; Ghate et al., 2021). Additionally, the prevalence of winter season precipitation-evaporation-

Deleted: 1Hz

Deleted: the too-

Deleted: 25Hz

Deleted: 20Hz

Deleted: winter

Deleted: the wintertime clouds feature

Deleted: summertime

Deleted: are elongated

Deleted: can

810 induced MBL cold pools, disturbs the MBL thermodynamics and contribute to turbulent mixing (Zuidema
 811 et al., 2017) can provide a strong dynamical forcing perturbation to the warm-rain process (Jenson et al.,
 812 2021; J. Wang et al., 2022; Smalley et al., 2024). The physical hypotheses from previous studies could
 813 potentially serve as the explanation for the phenomena that the ACE-ENA Win drizzle DSD is
 814 sufficiently broadened, and the D_{mmd} is enlarged toward the cloud base. In comparison, although the
 815 SOCRATES exhibits even thicker clouds (487.4 m), the drizzle processes are seemingly suppressed by
 816 the much higher ambient aerosol and CCN concentrations.

Deleted: , which disturb

Deleted:), during the wintertime might

Deleted: As a result,

Deleted: wintertime

817

818 4 Aerosol-cloud-precipitation interactions (ACPIs)

819 4.1 Cloud microphysical responses on aerosols

820 The impacts of aerosol loading on cloud microphysical properties can be assessed by the aerosol-
 821 cloud interaction (ACI) index, which can be quantified as both:

Deleted: different

Deleted: loadings

Deleted: the

Deleted: indices

$$822 ACI_N = \frac{\partial \ln(N_c)}{\partial \ln(N_{CCN,0.35\%})}, \quad (8)$$

823 and

$$824 ACI_r = -\frac{\partial \ln(r_c)}{\partial \ln(N_{CCN,0.35\%})}, \quad (9)$$

825 which emphasizes the cloud microphysical responses to CCN via the relative logarithmic change of N_c
 826 and r_c to the change in $N_{CCN,0.35\%}$ (Feingold et al., 2003; McComiskey et al., 2009). Physically, the ACI
 827 process involves aerosols intruding into the cloud layer, activating as cloud droplets, and subsequently
 828 altering cloud DSD and dispersion (Zheng et al., 2022a&b) under varying water vapor conditions.

Deleted: various

Deleted: availabilities

829 Therefore, the cloud microphysical responses within the lower region of the cloud are assessed, which is
 830 the first stage in which the sub-cloud CCN can directly interact with the cloud droplets. Furthermore, the
 831 similarity in the vertical integral of LWC_c (as shown in Fig. 3c) provides comparable liquid water
 832 between three IOPs for the assessment of newly generated cloud embryos from activated CCN because
 833 the ACI_r is normally assessed under a fixed liquid water (Zheng et al., 2020).

844 Considering all the cases from three IOPs with available CCN measurements (some cases without
845 CCN measurements during SOCRATES), the N_c and r_c at the lower cloud ($z_i < 0.2$) are plotted against
846 the sub-cloud $N_{CCN,0.35\%}$ in [Figures 6a and 6b](#), and the ACI indices are calculated as $ACI_{N, CB}$ and $ACI_{r, CB}$
847 (CB denoting the assessment near the cloud base). [The ACI indices from three IOPs are in the ACI range](#)
848 [of the previous studies in MBL clouds \(Twohy et al., 2005; Lu et al., 2009; Diamond et al., 2018\) using](#)
849 [aircraft in-situ measurements.](#) Note that the availability of valid sub-cloud measurements inevitably
850 limits the sample size, especially for SOCRATES, as shown in Table S2. As shown in Figure 6a, the
851 $ACI_{N, CB}$ for [ACE-ENA Win](#) (0.748) is higher than [ACE-ENA Sum](#) (0.617), indicating that N_c is more
852 sensitive to the sub-cloud $N_{CCN,0.35\%}$ during the winter. In other words, aerosols intruding into the cloud
853 layer are easily activated to become cloud droplets. The N_c sensitivity for the SOCRATES cloud (0.692)
854 lies between the two ACE-ENA IOPs. The $ACI_{N, CB}$ values from three IOPs are generally higher than the
855 ACI_N values from the layer-mean N_c against the sub-cloud $N_{CCN,0.35\%}$ (not shown). Previous studies have
856 shown that the enhanced vertical turbulence (updraft velocity) can effectively facilitate CCN
857 replenishment into the cloud layer (Hu et al., 2021; Zheng et al., 2022a&b) and increase the actual in-
858 cloud supersaturation (Brunke et al., 2022), thus leading to a more efficient cloud droplet formation,
859 enhancing the $ACI_{N, CB}$. By correlating the mean TKE values with the CCN activation ratio
860 ($N_c/N_{CCN,0.35\%}$) for all individual cloud cases, the three IOPs show moderate but statistically significant
861 correlation coefficients of 0.36, 0.55, and 0.51 for ACE-ENA [Sum](#), [ACE-ENA Win](#), and SOCRATES,
862 respectively. This result reinforces the notion that the CCN activation fractions, particularly during the
863 [ACE-ENA Win](#), are significantly correlated with in-cloud turbulence intensities. Furthermore, more
864 coarse mode aerosols during ACE-ENA [Win](#) are also favorable to the activation efficiency (Dusek et al.,
865 2006).

866 As for the r_c responses to CCN (Fig. 6b), the typical Twomey effect, where more CCN compete
867 against available water vapor and result in smaller cloud droplets, is [evident](#) by different cloud

Deleted: Figure 6

Moved (insertion) [2]

Deleted: the

Deleted: wintertime

Deleted: the summertime

Deleted: summer, winter

Deleted: wintertime

Deleted: winter

Deleted: evidenced

876 susceptibility between the three IOPs. SOCRATES features a higher $ACI_{r, CB}$ (0.311), suggesting that an
 877 increase in $N_{CCN, 0.35\%}$ can result in a significant decrease in r_c , compared to ACE-ENA Sum (0.206) and
 878 ACE-ENA Win (0.263). Although the absolute range of variation for r_c during SOCRATES is smaller,
 879 the slope is much deeper (Fig. 6b). Recall that the sub-cloud $N_{CCN, 0.35\%}$ during SOCRATES is generally
 880 higher than ACE-ENA and contains more small-sized aerosols (as indicated in Fig. 2b). Consequently,
 881 after activation, the lower part of the cloud exhibits a higher number of smaller cloud droplets for
 882 SOCRATES, as shown in Fig. 4d. Therefore, as more CCN intrudes into the cloud, the competition for
 883 water vapor among newly-activated cloud droplets becomes more pronounced, given similar water
 884 availability. In contrast, the presence of larger cloud droplets near the cloud base, whether activated from
 885 coarse-mode aerosols or remaining as residuals from collision-coalescence, would elevate the r_c
 886 especially under the relatively less CCN condition, hence inevitably dampening the $ACI_{r, CB}$ during ACE-
 887 ENA. However, a more comprehensive investigation into the cloud microphysical responses to CCN
 888 intrusions under a larger range of various water supply conditions, and further untangling the ACI from
 889 the meteorological influences, will require additional aircraft cases from more field campaigns. Examples
 890 include, the VAMOS Ocean-Cloud-Atmosphere-Land Study (VOCALS; [Wood et al., 2011](#)), the Cloud
 891 System Evolution over the Trades (CSET; [Albrecht et al., 2019](#)), the ObseRvations of CLouds above
 892 Aerosols and their intEractionS (ORACLES; [Redemann et al., 2021](#)), and the Aerosol Cloud
 893 meTeorology Interactions oVer the western ATlantic Experiment (ACTIVATE; [Sorooshian et al., 2019](#)).
 894 Note that the $ACI_{r, CB}$ values in Figure 6b are also larger than the results from the layer-mean r_c against
 895 sub-cloud $N_{CCN, 0.35\%}$, since the layer-mean microphysics is more subject to the cloud droplet evolution
 896 processes such as condensational growth and collision-coalescence.

897 To investigate the ACI indices at the upper level of the cloud, the N_c and r_c at the upper cloud
 898 ($z_i > 0.8$) are plotted against the above-cloud $N_{CCN, 0.35\%}$ in [Figures 6c and 6d](#), and the ACI indices are
 899 calculated as $ACI_{N, CT}$ and $ACI_{r, CT}$ (denoting the assessments near the cloud top). Compared to the

Deleted: The

Deleted: summer

Deleted: winter

Deleted: is constituted by

Deleted: , even under the relatively less $N_{CCN, 0.35\%}$ condition for SOCRATES...

Deleted: more

Deleted: , for instance

Moved up [2]: The ACI indices from three IOPs are in the ACI range of the previous studies in MBL clouds (Twohy et al., 2005; Lu et al., 2009; Diamond et al., 2018) using aircraft in-situ measurements.

Deleted: Figure S5

913 $ACI_{N,CB}$ and $ACI_{r,CB}$, the $ACI_{N,CT}$ and $ACI_{r,CT}$ are much weaker, especially for $ACI_{r,CT}$, as the near cloud
 914 top droplets are too large for above-cloud aerosols to exert a significant influence on r_c (Diamond et al.,
 915 2018; Gupta et al., 2022). The weaker cloud top N_c dependence on the $N_{CCN,0.35\%}$ could be due to the
 916 legacy of the sub-cloud CCN impacts on N_c being conveyed to the cloud top. This occurs because FT
 917 aerosols and CCN can be entrained into the MBL before and during the cloud process, as observed in the
 918 assessment of inter-cloud cases. Note that the LWC_c near the cloud top for the three IOPs are not
 919 comparable to each other, which might also induce uncertainty in the near-cloud-top ACI assessment.
 920 These weaker relationships support the notion that although the aerosols entrained into the upper-cloud
 921 region can affect the cloud microphysics to a certain degree, the effects are less pronounced than those
 922 from the sub-cloud aerosols (Diamond et al., 2018, Wang et al., 2020) because the MBL cloud N_c and r_c
 923 variations are dominated by the condensational growth, collision-coalescence, and entrainment mixing
 924 processes near the cloud top.

Deleted: While the

Deleted: down to

926 4.2 Precipitation susceptibility

927 The precipitation susceptibility relies on the assessment of relative responses in the precipitation
 928 rate to the change in N_c (Feingold and Seibert, 2009; Sorooshian et al., 2009), which is defined as:

$$929 S_o = -\frac{\partial \ln(R_{CB})}{\partial \ln(N_c)}, \quad (10)$$

930 where the R_{CB} is the cloud base precipitation rate calculated in section 2 (equation 5). By incorporating
 931 all the cloud cases, including both precipitating and non-precipitating clouds (the R_{CB} can also be
 932 calculated based on the drizzle DSD near the cloud base), the S_o accounts for the impact of cloud droplets
 933 on the potential precipitation ability of the cloud (Terai et al., 2012).

934 As shown in Figure 7a, the R_{CB} values generally have a negative correlation with increased layer-
 935 mean N_c for all three IOPs. The S_o values are 0.979, 1.229, and 1.638, with the absolute values of
 936 correlation coefficients being 0.33, 0.29, and 0.45 for SOCRATES, ACE-ENA Sum, and ACE-ENA Win,

Deleted: summer

Deleted: winter

941 respectively. The regression relationships are statistically significant with $p < 0.05$ for all three IOPs.
 942 These correlation coefficient values fall within the reasonable range found in previous studies on
 943 precipitation susceptibility in MBL stratus and stratocumulus clouds (Jung et al., 2016; Gupta et al.,
 944 2022), and indicate statistically significant dependences of R_{CB} on N_c . Previous study by Terai et al.
 945 (2012) found that the S_o values decrease with the increasing cloud thickness over the southeast Pacific,
 946 and Jung et al. (2016) found that the S_o is more pronounced within the medium-deep clouds with
 947 thickness ~ 300 -400 m in the MBL stratocumulus over the eastern Pacific. Gupta et al. (2022) found that
 948 the S_o values are generally higher under low ambient N_a condition in the southeastern Atlantic MBL. In
 949 this study, R_{CB} for the ACE-ENA Win is more susceptible to the layer-mean N_c than the ACE-ENA Sum
 950 and SOCRATES, which can be partially attributed to the existence of more large drizzle drops (as shown
 951 in Fig. 4d) near the cloud base in ACE-ENA Win. As previously discussed, the ACE-ENA Win featured
 952 enhanced collision-coalescence suggested by the stronger in-cloud turbulence, and a possible drizzle-
 953 recirculating process as indicated by the previous study. And such mechanisms might explain the low N_c
 954 conditions with more large drizzle drops, leading to the increase of S_o values during ACE-ENA Win. In
 955 comparison, the aerosol of SOCRATES is largely composed of fine Aitken mode aerosol, which results
 956 in smaller cloud droplets. Thus, collision-coalescence is ineffective during SOCRATES, which leads to
 957 the relatively narrower drizzle DSDs, where the warm-rain processes are suppressed, and in turn,
 958 diminishing the sensitivity of R_{CB} to N_c (Stevens and Feingold, 2009; Fan et al., 2020; Gupta et al., 2022).

959 It is well known that the R_{CB} can be parameterized or predicted by assuming an approximate
 960 relation with N_c and cloud thickness (H_c), which is usually parameterized in the form of $R_{CB} \propto c H_c^3 N_c^{-1}$
 961 (Lu et al., 2009; Kang et al., 2024). Following the same method, we derive the relationships from three
 962 IOPs in Figure 7b, where the R_{CB} are positively (negatively) proportional to the H_c (N_c), with the
 963 exponential parameters in the range of the typical values in the MBL clouds (Comstock et al., 2004; van
 964 Zanten et al., 2005; Lu et al., 2009). The statistical coefficient of determination (R^2) values of R_{CB} against

Deleted: While

Deleted: winter

Deleted: summer

Deleted: .

Deleted: winter

Deleted: processes, especially under

Deleted: .

Deleted: higher ambient

Deleted: and CCN concentrations during

Deleted: lead

Deleted: and may induce effective aerosol buffering effects

Deleted: in cloud

Deleted: already fairly

Deleted: hence

Deleted: via

Deleted: vanZanten

981 H_c (N_c) are 0.696 (0.177), 0.419 (0.212) and 0.165 (0.295), for the ACE-ENA ~~Sum~~, winter and
982 SOCRATES, respectively, suggesting that the R_{CB} in ACE-ENA clouds may be more determined by H_c ,
983 while the R_{CB} in SOCRATES ~~clouds could be less dependent on both H_c and N_c~~ . Note that the
984 relationship for SOCRATES in this study reveals a similar R_{CB} dependence on N_c but a smaller
985 dependence on the cloud thickness than the study by Kang et al. (2024), who concluded a relationship of
986 $R_{CB} = 1.41 \times 10^{-9} H_c^{3.1} N_a^{-0.8}$, based on the rain rate retrieved from radar and lidar measurements and
987 the aerosol concentration also from the SOCRATES. The discrepancies are possibly due to the different
988 sample selections and different methods in the R_{CB} calculation. Note that the mean cloud thicknesses of
989 ~~ACE-ENA Sum~~ (336.3 m), ~~ACE-ENA Win~~ (392.4 m) and SOCRATES (487.4 m), are within the
990 thickness range found to exhibit stronger S_o (Terai et al., 2012; Jung et al., 2016; Gupta et al., 2022).

Deleted: summer

Deleted: cloud are more related to

Deleted: the

Deleted: summer

Deleted: winter

993 4.3 Drizzle impacts on sub-cloud CCN and implication to ACI

994 Multiple studies on the MBL clouds have concluded that the in-cloud drizzle formation and
995 evolution processes can effectively impact the sub-cloud CCN budgets via the coalescence-scavenging
996 effect (Wood, 2006; Wood et al., 2012; Diamond et al., 2018; Zheng et al., 2022b; Zhang et al., 2023).
997 Drizzle drops are formed and grow via the collision-coalescence process by collecting cloud droplets and
998 small drizzle drops, resulting in the consumption of CCN (the precursor of cloud droplet), but in the
999 meantime, the in-cloud N_c can be continuously buffered by the sub-cloud CCN replenishment. Although
1000 the sub-cloud aerosols (especially in large size) would be added if the drizzle fell and evaporated outside
1001 the cloud, the increment cannot compensate for the loss. Therefore, the net result of the whole process is
1002 usually presented as the depletion of sub-cloud CCN residuals, and such drizzle modulation on the CCN
1003 budget could be substantial in moderate-to-light drizzles or even non-precipitating clouds, depending on
1004 the collision-coalescence efficiency (Feingold et al., 1996; Wood, 2006; Kang et al., 2022).

The CCN loss rate due to the coalescence-scavenging effect can be calculated as:

$$L_{CCN} = -\frac{K H_c}{H_{cp}} * N_c * R_{CB}, \quad (11)$$

where the constant K ($2.25 \text{ m}^2 \text{ kg}^{-1}$) denotes the drizzle collection efficiency (Wood et al., 2006; Diamond et al., 2018). H_c is cloud thickness, and H_{cp} is the coupled layer thickness to ensure the change in the cloud layer can be sufficiently conveyed throughout the layer. The calculated CCN loss rate for individual cases is listed in Table S2. Considering all cloud (precipitating cloud) scenarios, the mean CCN loss rates are $-7.69 \pm 13.96 \text{ cm}^{-3} \text{ h}^{-1}$ ($-10.45 \pm 15.56 \text{ cm}^{-3} \text{ h}^{-1}$), $-6.29 \pm 11.65 \text{ cm}^{-3} \text{ h}^{-1}$ ($-12.11 \pm 14.64 \text{ cm}^{-3} \text{ h}^{-1}$), and $-4.94 \pm 7.96 \text{ cm}^{-3} \text{ h}^{-1}$ ($-5.58 \pm 8.43 \text{ cm}^{-3} \text{ h}^{-1}$) for ACE-ENA Sum, ACE-ENA Win and SOCRATES, respectively. As the results indicate, the ACE-ENA clouds experience a more substantial sub-cloud CCN loss than SOCRATES, especially in wintertime precipitating clouds. Recall that the assessment of $ACI_{r,CB}$ relies on the relative changes of r_c and N_{CCN} , while the different L_{CCN} for individual cases can result in the shrinking of the N_{CCN} variation ranges (imagine the abundant CCN are depleted by the coalescence-scavenging). In other words, the given change in r_c corresponds to a narrowed change in N_{CCN} . Mathematically speaking, the assessment of $ACI_{r,CB}$ depends on the ratio of the numerator (change in r_c) and the denominator (change in N_{CCN}). Under the circumstances of substantial cloud-processing to the aerosols, the altered sub-cloud CCN budgets are reflected as a smaller denominator, versus the less altered numerator, hence mathematically presented as an enlarged $ACI_{r,CB}$. Therefore, the coalescence-scavenging effect can not only deplete the sub-cloud CCN, but also quantitatively amplify the assessment of cloud microphysics susceptibilities (Feingold et al., 1999; Duong et al., 2011; Jung et al., 2016; Zheng et al., 2022b). In order to examine the potential impact of the aforementioned processes on the ACI assessment, a sensitivity analysis is conducted by simply retrospectively the sub-cloud $N_{CCN0.35\%}$ according to their L_{CCN} . For each retrospective time step ΔT , the r_c values are held unchanged, and the retrospective $N_{CCN0.35\%}$ values for individual cloud cases are given by $N_{CCN0.35\%} - L_{CCN} * \Delta T$, and then the $ACI_{r,CB}$ can be recalculated. Note that assuming a constant r_c value over time inevitably induces

Deleted: 3h

Deleted: 3h

Deleted: 3h

Deleted: 3h

Deleted: 3h

Deleted: 3h

Deleted: summer, winter

1041 uncertainty and biases, as it does not consider the microphysical processes affecting the cloud droplet
1042 mean size. However, previous numerical experiments show that the noticeable impact on the cloud mean
1043 radius through collision-coalescence necessitates a high degree of CCN depletion, and the quantified
1044 percentage changes in droplet mean sizes are several times less than the changes in CCN depletion
1045 (Feingold et al., 1996). Hence, the retrospective method, from an observational snapshot point of view,
1046 provides a direction that enables the assessment of $ACI_{r, CB}$ as if before the sub-cloud aerosols and CCN
1047 are scavenged by in-cloud coalescence-scavenging and precipitation scavenging processes.

1048 As shown in Figure 8, the $ACI_{r, CB}$ values tend to decrease with the retrospective time, which
1049 indicates the retrospective CCN variation range is enlarged and counteracting the coalescence-
1050 scavenging amplification. The detailed illustration of the different $ACI_{r, CB}$ calculated from the scattered
1051 r_c and sub-cloud $N_{CCN0.35\%}$ is shown in Figure S5. Note that the $ACI_{r, CB}$ decreasing rates for the
1052 precipitating clouds (Fig. 8b) are not as strong as for all clouds because the non-precipitating clouds have
1053 smaller L_{CCN} largely due to weaker collision-coalescence. Hence, the retrospective period used here
1054 might quickly exceed the actual time of cloud-processing to become effective on aerosol and CCN. In
1055 other words, the actual time needed, to trace back to the sub-cloud CCN concentration before they were
1056 cloud-processed, is shorter, than the retrospective time tested here in Figure 8. This results in the faster
1057 decrease of $ACI_{r, CB}$ in the non-precipitating cloud. The retrospective of the sub-cloud CCN budget will
1058 yield an alternative assessment of ACI, assuming that the drizzle processes have not yet significantly
1059 impacted the sub-cloud CCN budget, especially for the assessment under the precipitating clouds.
1060 However, examining the exact precipitating timing is challenging since the aircraft provides a snapshot
1061 of the cloud and aerosol information. Thus, this retrospective study only provides a possible direction,
1062 and the result should be interpreted with caution.

1063

1064

Deleted: S6

Deleted: time scale

Deleted: the

Deleted: effects

Deleted: the

Deleted: ,

Deleted: restore

Deleted: to the budget

Deleted: the

Deleted: processing

Deleted: . Thus,

1076 **5. Summary and Conclusions**

1077 Based on the aircraft in-situ measurements during ACE-ENA and SOCRATES, the vertical
1078 distributions and the evolutions of the aerosol, cloud, and drizzle properties are investigated under cloud-
1079 topped MBL environments. The aerosols and CCN from SOCRATES are the highest among the three
1080 IOPs, followed by ACE-ENA ~~Sum~~, and ~~ACE-ENA Win~~ in descending order in both above- and sub-
1081 cloud regimes. The differences can be attributed to the differences in aerosol size distributions between
1082 ACE-ENA and SOCRATES, which are largely due to the aerosol sources in those regions. The
1083 SOCRATES features the pre-industrial natural environment enriched by aerosols from marine biological
1084 productivity and without the contamination of anthropogenic aerosols, while the ACE-ENA features the
1085 aerosols from varied sources, including maritime and continental emissions, with distinct seasonal
1086 variations. Examining the aerosol size distributions in sub-cloud versus above-cloud regimes manifests
1087 the significant influence of cloud processing on aerosols. ~~According to previous studies, physical~~
1088 processing like in-cloud Brownian capture can reduce Aitken mode aerosols, while the chemical
1089 processes transform Aitken mode aerosols to larger sizes, moving them toward the accumulation mode.
1090 In addition, the in-cloud coalescence processes ~~could also~~ shift sub-cloud aerosol residuals to larger sizes,
1091 as multiple aerosols combine into a single aerosol core inside the cloud droplet during collision-
1092 coalescence. ~~Those physical mechanisms could potentially explain~~ the observed increase in the tail of
1093 the aerosol ~~size~~ distribution for all IOPs, ~~and it will be of interest for future research to prove such~~
1094 ~~hypotheses~~.

1095 As for the cloud and drizzle properties, the SOCRATES clouds feature ~~a larger number of~~ smaller
1096 cloud droplets than the ACE-ENA ~~Sum~~ and ~~ACE-ENA Win~~ clouds, with the r_c ~~growth~~ (and ~~percent~~
1097 increases), from cloud base to top, being 4.03 μm (0.66%), 4.78 μm (0.68%), and 5.85 μm (0.79%) for
1098 SOCRATES, ACE-ENA ~~Sum~~, and ~~ACE-ENA Win~~, respectively. The cloud-top entrainment mixing is
1099 ~~evident~~ in the observed decline of both N_c and LWC_c near the cloud top. The mean cloud-top entrainment
1100 rates (w_e) are $0.570 \pm 0.834 \text{ cm s}^{-1}$, $0.581 \pm 0.560 \text{ cm s}^{-1}$, and $0.960 \pm 1.127 \text{ cm s}^{-1}$ for SOCRATES, ACE-

Deleted: the

Deleted: summer

Deleted: winter

Deleted: Physical

Deleted: , explaining

Deleted: -end

Deleted: more and

Deleted: summertime

Deleted: wintertime

Deleted: growths

Deleted: percentage

Deleted: summer

Deleted: winter

Deleted: evidenced

1115 ENA, Sum, and ACE-ENA Win, respectively. The strongest w_e during ACE-ENA Win is a result of
 1116 weaker cloud-top inversions and stronger near-cloud-top turbulence. The values of the TKE for three
 1117 IOPs are generally within the ranges of previous studies (Atlas et al., 2020; Ghate et al., 2021). For drizzle
 1118 vertical distribution, N_d from the three IOPs all exhibit decreases from cloud top to cloud base, while
 1119 D_{mmd} are in opposite directions with a maximum at the cloud base. The ACE-ENA Win clouds feature
 1120 more prominent drizzle formation and evolution owing to the combined effects of relatively cleaner
 1121 environment, deeper cloud layer, and slightly stronger in-cloud vertical turbulence, which is speculated
 1122 to substantially enhance the collision-coalescence and the drizzle re-circulating processes, compared to
 1123 the other two IOPs. Satellite retrievals of droplet number concentration heavily rely on the adiabatic
 1124 cloud assumption and are usually given as a constant of $f_{ad} = 0.8$, the in-situ observational evidence
 1125 found in this study further confirms the unrealistic nature of this assumption. It will be of interest to
 1126 utilize multiple aircraft measurements (campaigns) to explore the variability of MBL cloud and drizzle
 1127 microphysical properties over different marine regions. This can help examine potential predictors for
 1128 f_{ad} , which will aid in satellite-based retrievals and aerosol-cloud interaction assessments (Painemal and
 1129 Zuidema, 2011; Grosvenor et al., 2018; Painemal et al., 2021).

1130 Comparing the seasonality of cloud-base precipitation rate (R_{CB}) during ACE-ENA, more cases
 1131 with large observed R_{CB} during the winter season, which is consistent with J. Wang et al. (2022). Notably,
 1132 the sensitivity of R_{CB} to N_c is more pronounced for the ACE-ENA during both winter (with precipitation
 1133 susceptibility $S_o = 1.638$) and summer ($S_o = 1.229$) compared to the SOCRATES ($S_o = 0.979$). This
 1134 could be possibly hypothesized as the result of turbulence-driven in-cloud droplet interactions, which
 1135 could result in much higher R_{CB} induced by larger drizzle drops near the cloud base for ACE-ENA,
 1136 especially under low N_c conditions. Furthermore, R_{CB} can be approximated by a relationship involving
 1137 N_c and H_c , as suggested in prior research. The relationships established in this study indicate that the S_o
 1138 in ACE-ENA clouds can be partially determined by H_c , while in SOCRATES clouds the S_o is less

Deleted: summer
 Deleted: winter
 Deleted: winter
 Deleted: owing to

Deleted: wintertime

Deleted: enhances

Deleted: While satellite

Deleted:

Deleted: is partly due to the

Deleted: a result of turbulence-driven in-cloud droplet interactions, ...

Deleted: condition

Deleted: , are largely

Deleted: are more

1153 influenced by H_c and N_c . ~~Based on the physical mechanisms found in the previous study, a possible~~
1154 ~~hypothesis can be leveraged to explain the observed results. That is, the~~ combination of a deeper cloud
1155 layer and relatively lower ambient aerosol concentration, eventually leading to stronger drizzle
1156 production and evolution during ACE-ENA, especially during the winter season, results in more robust
1157 precipitation susceptibility. ~~And further numerical simulations and experiments are warranted to prove~~
1158 ~~this hypothesis.~~ Note that considering the combined factors of aerosol loadings, cloud morphology and
1159 thicknesses, and the assessment methodology, the derived S_o values in this study are generally higher (or
1160 close to the upper end) compared to previous studies (Lu et al., 2009; Duong et al., 2011; Terai et al.,
1161 2012; Jung et al., 2016; Gupta et al., 2022).

1162 The investigations of the ACI via the $ACI_{N, CB}$ and $ACI_{r, CB}$ indices reveal that during the ACE-
1163 ENA ~~Win~~, N_c is more sensitive to changes in $N_{CCN0.35\%}$, indicating aerosols more readily activate to
1164 become cloud droplets compared to those in the ~~ACE-ENA Sum~~, which is consistent with the previous
1165 assessment by J. Wang et al. (2022) on the seasonal dependency of the relationship between N_c and
1166 aerosols. One influencing factor is the strong dynamic mechanism that speeds up the infusion of CCN
1167 into the cloud layer, thus aiding droplet formation. The moderate but statistically significant correlation
1168 coefficients between the CCN activation fractions and the TKE agree with a previous study that found
1169 the local activation fraction of CCN to be strongly associated with increased updrafts (Hu et al., 2021).
1170 Furthermore, the presence of larger aerosols during ACE-ENA ~~Win~~ enhances the droplet activation
1171 process. The SOCRATES IOP highlights a higher $ACI_{r, CB}$, indicating a pronounced decrease in r_c with
1172 increasing $N_{CCN0.35\%}$. The $ACI_{r, CB}$ in ACE-ENA is dampened by the presence of more large cloud
1173 droplets near the cloud base, particularly under relatively higher $N_{CCN0.35\%}$. However, the combined
1174 effect of the relatively cleaner environment and sufficient water vapor results in stronger cloud
1175 microphysical responses during the ACE-ENA wintertime than in the summertime. Note that the ACI
1176 indices from this study lie in the higher end of the ACI ranges estimated via remote sensing (McComiskey

Deleted: the

Deleted: The

Deleted: wintertime

Deleted: summer

Deleted: winter

1182 et al., 2009; Dong et al., 2015; Zheng et al., 2022a) possibly because the aircraft assessment of ACI is
1183 based on measurements where the aerosols are in direct contact with the cloud layer. Arguably, the
1184 assessment of N_c responses to $N_{CCN0.35\%}$ would inevitably be affected by the collision-coalescence
1185 process near the cloud base, where simultaneously, the CCN replenishment buffers the N_c and the
1186 collision-coalescence process depletes N_c . Hence, finding a layer where these two effects maintain a
1187 dynamic balance in N_c might aid in a more accurate assessment and more fundamental understanding of
1188 the ACI, which might be revealed by the LES or parcel model simulations.

1189 Additionally, the in-cloud drizzle formation and evolution processes significantly influence the
1190 sub-cloud CCN budgets via the coalescence-scavenging effect, which can potentially exaggerate the
1191 assessment of cloud microphysics susceptibilities. Based on the CCN loss rate (L_{CCN}) from ACE-ENA
1192 and SOCRATES, a sensitivity analysis is performed focusing on retrospectively adjusting the sub-cloud
1193 CCN according to their L_{CCN} . Results showed that this adjustment led to a decreased $ACI_{r,CB}$,
1194 highlighting the significance of the coalescence-scavenging process on the ACI assessment. However,
1195 due to the fact that aircraft only provide a snapshot of the clouds and aerosol information, determining
1196 the precise drizzle timing for the individual cloud is challenging. Hence, findings from this retrospective
1197 approach provide only a direction or theory, and should be taken cautiously. Nevertheless, pursuing
1198 further modeling experiments on this matter may be worthwhile. For example, the exact drizzling time
1199 could be pinpointed within a model using an Eulerian framework or traced using a Lagrangian framework.
1200 Nevertheless, the CCN adjustment could more accurately reflect the true characteristics of the cloud and
1201 the MBL CCN budget, potentially aiding in a more precise assessment of ACI. Therefore, future research
1202 would focus on model simulations of MBL clouds from ACE-ENA and SOCRATES and further assess
1203 the modeled ACI under the observational constraints, as well as the continuous development of the warm
1204 rain microphysical parameterizations, in order to aid in the better represent the MBL clouds in multiple
1205 regions.

Deleted: works

Deleted: the

Deleted: simulation on the

1209

Deleted: ¶

1210 *Data availability.* The ACE-ENA field campaign data can be accessed from the Department of Energy
1211 Atmospheric Radiation Measurement data archive (<https://iop.archive.arm.gov/arm-iop->
1212 [file/2017/ena/aceena/](https://iop.archive.arm.gov/arm-iop-file/2017/ena/aceena/)). The SOCRATES field campaign data are publicly archived on the National
1213 Center for Atmospheric Research (NCAR) Earth Observing Laboratory
1214 (https://data.eol.ucar.edu/master_lists/generated/socrates/).

1215

1216 *Author contributions.* The original idea of this study is discussed by XZ, XD, and BX. XZ performed the
1217 analyses and wrote the manuscript. XZ, XD, BX, TL, and YW participated in further scientific
1218 discussions and provided substantial comments and edits on the paper.

1219

1220 *Competing interests.* At least one of the (co-)authors is a member of the editorial board of Atmospheric
1221 Chemistry and Physics.

1222

1223 *Acknowledgments.* This work was supported by the NSF grants AGS-2031750/2031751/20211752 at the
1224 University of Arizona, Texas A&M University and Stanford University, respectively. The authors
1225 sincerely thank the investigators and mentors from the ACE-ENA and SOCRATES field campaigns for
1226 making the data publicly available.

1227

1228 **References.**

1229 Albrecht B. A.: Aerosols, Cloud Microphysics, and Fractional Cloudiness, *Science*, 245, 1227-1230,
1230 [10.1126/science.245.4923.1227](https://doi.org/10.1126/science.245.4923.1227), 1989

1231 Albrecht, B. A., Bretherton, C. S., Johnson, D., Scubert, W. H., and Frisch, A. S.: The Atlantic
1232 Stratocumulus Transition Experiment—ASTEX, *B. Am. Meteorol. Soc.*, 76, 889-904,
1233 [10.1175/1520-0477\(1995\)076<0889:Taste>2.0.Co;2](https://doi.org/10.1175/1520-0477(1995)076<0889:Taste>2.0.Co;2), 1995.

1235 Albrecht, B., Fang, M., and Ghate, V.: Exploring Stratocumulus Cloud-Top Entrainment Processes and
1236 Parameterizations by Using Doppler Cloud Radar Observations, *J. Atmos. Sci.*, 73, 729-742,
1237 10.1175/JAS-D-15-0147.1, 2016.

1238 [Albrecht, B., Ghate, V., Mohrmann, J., Wood, R., Zuidema, P., Bretherton, C., Schwartz, C., Eloranta,](#)
1239 [E., Glienke, S., Donaher, S., Sarkar, M., McGibbon, J., Nugent, A. D., Shaw, R. A., Fugal, J.,](#)
1240 [Minnis, P., Paliknoda, R., Lussier, L., Jensen, J., Vivekanandan, J., Ellis, S., Tsai, P., Rilling, R.,](#)
1241 [Haggerty, J., Campos, T., Stell, M., Reeves, M., Beaton, S., Allison, J., Stossmeister, G., Hall, S.,](#)
1242 [and Schmidt, S.: Cloud System Evolution in the Trades \(CSET\): Following the Evolution of](#)
1243 [Boundary Layer Cloud Systems with the NSF-NCAR GV. *B. Am. Meteorol. Soc.*, 100, 93-121,](#)
1244 <https://doi.org/10.1175/BAMS-D-17-0180.1>, 2019.

1245 Atlas, R. L., Bretherton, C. S., Blossey, P. N., Gettelman, A., Bardeen, C., Lin, P., and Ming, Y.: How
1246 Well Do Large-Eddy Simulations and Global Climate Models Represent Observed Boundary Layer
1247 Structures and Low Clouds Over the Summertime Southern Ocean?, *Journal of Advances in*
1248 *Modeling Earth Systems*, 12, e2020MS002205, <https://doi.org/10.1029/2020MS002205>, 2020.

1249 Atlas, R., Mohrmann, J., Finlon, J., Lu, J., Hsiao, I., Wood, R., and Diao, M.: The University of
1250 Washington Ice-Liquid Discriminator (UWILD) improves single-particle phase classifications of
1251 hydrometeors within Southern Ocean clouds using machine learning, *Atmos. Meas. Tech.*, 14,
1252 7079-7101, 10.5194/amt-14-7079-2021, 2021.

1253 Baumgardner, D. and Korolev, A.: Airspeed Corrections for Optical Array Probe Sample Volumes, *J.*
1254 *Atmos. Ocean. Tech.*, 14, 1224-1229, [https://doi.org/10.1175/1520-](https://doi.org/10.1175/1520-0426(1997)014<1224:ACFOAP>2.0.CO;2)
1255 [0426\(1997\)014<1224:ACFOAP>2.0.CO;2](https://doi.org/10.1175/1520-0426(1997)014<1224:ACFOAP>2.0.CO;2), 1997.

1256 Baumgardner, D., Abel, S. J., Axisa, D., Cotton, R., Crosier, J., Field, P., Gurganus, C., Heymsfield, A.,
1257 Korolev, A., Krämer, M., Lawson, P., McFarquhar, G., Ulanowski, Z., and Um, J.: Cloud Ice
1258 Properties: In Situ Measurement Challenges, *Meteor. Monogr.*, 58, 9.1-9.23,
1259 <https://doi.org/10.1175/AMSMONOGRAPHS-D-16-0011.1>, 2017.

1260 Braun, R. A., Dadashazar, H., MacDonald, A. B., Crosbie, E., Jonsson, H. H., Woods, R. K., Flagan, R.
1261 C., Seinfeld, J. H., and Sorooshian, A.: Cloud Adiabaticity and Its Relationship to Marine
1262 Stratocumulus Characteristics Over the Northeast Pacific Ocean, *J. Geophys. Res.-Atmos.*, 123,
1263 13790 - 13806, 10.1029/2018jd029287, 2018.

1264 Brenguier, J. L., Burnet, F., and Geoffroy, O.: Cloud optical thickness and liquid water path – does the k
1265 coefficient vary with droplet concentration?, *Atmos. Chem. Phys.*, 11, 9771-9786, 10.5194/acp-11-
1266 9771-2011, 2011.

1267 Brost, R. A., Wyngaard, J. C., and Lenschow, D. H.: Marine Stratocumulus Layers. Part II: Turbulence
1268 Budgets, *J. Atmos. Sci.*, 39, 818-836, 10.1175/1520-0469(1982)039<0818:MSLPIT>2.0.CO;2,
1269 1982.

1270 Brunke, M. A., Cutler, L., Urzua, R. D., Corral, A. F., Crosbie, E., Hair, J., Hostetler, C., Kirschler, S.,
1271 Larson, V., Li, X.-Y., Ma, P.-L., Minke, A., Moore, R., Robinson, C. E., Scarino, A. J., Schlosser,
1272 J., Shook, M., Sorooshian, A., Lee Thornhill, K., Voigt, C., Wan, H., Wang, H., Winstead, E., Zeng,
1273 X., Zhang, S., and Ziemba, L. D.: Aircraft Observations of Turbulence in Cloudy and Cloud-Free
1274 Boundary Layers Over the Western North Atlantic Ocean From ACTIVATE and Implications for
1275 the Earth System Model Evaluation and Development, *J. Geophys. Res.-Atmos.*, 127,
1276 e2022JD036480, <https://doi.org/10.1029/2022JD036480>, 2022.

1277 Chen, J., Liu, Y., Zhang, M., and Peng, Y.: Height Dependency of Aerosol-Cloud Interaction Regimes,
1278 *J. Geophys. Res.-Atmos.*, 123, 491-506, <https://doi.org/10.1002/2017JD027431>, 2018.

1279 Chen, S., Yau, M. K., and Bartello, P.: Turbulence Effects of Collision Efficiency and Broadening of
1280 Droplet Size Distribution in Cumulus Clouds, *J. Atmos. Sci.*, 75, 203-217,
1281 <https://doi.org/10.1175/JAS-D-17-0123.1>, 2018.

1282 Chen, Y. C., Xue, L., Lebo, Z. J., Wang, H., Rasmussen, R. M., and Seinfeld, J. H.: A comprehensive
1283 numerical study of aerosol-cloud-precipitation interactions in marine stratocumulus, *Atmos. Chem.*
1284 *Phys.*, 11, 9749-9769, 10.5194/acp-11-9749-2011, 2011.

1285 Christensen, M. W., Ma, P. L., Wu, P., Varble, A. C., Mülmenstädt, J., and Fast, J. D.: Evaluation of
1286 aerosol–cloud interactions in E3SM using a Lagrangian framework, *Atmos. Chem. Phys.*, 23, 2789-
1287 2812, 10.5194/acp-23-2789-2023, 2023.

1288 Comstock, K. K., Wood, R., Yuter, S. E., and Bretherton, C. S.: Reflectivity and rain rate in and below
1289 drizzling stratocumulus, *Q. J. R. Meteor. Soc.*, 130, 2891-2918, <https://doi.org/10.1256/qj.03.187>,
1290 2004.

1291 Cooper, W. A., Friesen, R. B., Hayman, M., Jensen, J., Lenschow, D. H., Romashkin, P., Schanot, A., Spuler, S.,
1292 Stith, J., and Wolff, C.: Characterization of Uncertainty in Measurements of Wind from the NSF/NCAR
1293 Gulfstream V Research Aircraft (No. NCAR/TN-528+STR), NCAR Technical Notes,
1294 doi:10.5065/D60G3HJ8, 2016.

1295 Covert, D. S., Kapustin, V. N., Bates, T. S., and Quinn, P. K.: Physical properties of marine boundary
1296 layer aerosol particles of the mid-Pacific in relation to sources and meteorological transport, *J.*
1297 *Geophys. Res.-Atmos.*, 101, 6919-6930, <https://doi.org/10.1029/95JD03068>, 1996.

1298 D'Alessandro, J. J., McFarquhar, G. M., Wu, W., Stith, J. L., Jensen, J. B., and Rauber, R. M.:
1299 Characterizing the Occurrence and Spatial Heterogeneity of Liquid, Ice, and Mixed Phase Low-
1300 Level Clouds Over the Southern Ocean Using in Situ Observations Acquired During SOCRATES,
1301 *J. Geophys. Res.-Atmos.*, 126, e2020JD034482, <https://doi.org/10.1029/2020JD034482>, 2021.

1302 Danker, J., Sourdeval, O., McCoy, I. L., Wood, R., and Possner, A.: Exploring relations between cloud
1303 morphology, cloud phase, and cloud radiative properties in Southern Ocean's stratocumulus clouds,
1304 *Atmos. Chem. Phys.*, 22, 10247-10265, 10.5194/acp-22-10247-2022, 2022.

1305 Desai, N., Liu, Y., Glienke, S., Shaw, R. A., Lu, C., Wang, J., and Gao, S.: Vertical Variation of Turbulent
1306 Entrainment Mixing Processes in Marine Stratocumulus Clouds Using High-Resolution Digital
1307 Holography, *J. Geophys. Res.-Atmos.*, 126, e2020JD033527,
1308 <https://doi.org/10.1029/2020JD033527>, 2021.

1309 Dong, X., Schwantes, A. C., Xi, B., and Wu, P.: Investigation of the marine boundary layer cloud and
1310 CCN properties under coupled and decoupled conditions over the Azores, *J. Geophys. Res.-Atmos.*,
1311 120, 6179-6191, <https://doi.org/10.1002/2014JD022939>, 2015.

1312 Dong, X., X. Zheng, B. Xi, and S. Xie (2023), A Climatology of Midlatitude Maritime Cloud Fraction
1313 and Radiative Effect Derived from the ARM ENA Ground-Based Observations, *J. Climate*, 36(2),
1314 531-546, doi:10.1175/JCLI-D-22-0290.1.

1315 Duong, H. T., Sorooshian, A., and Feingold, G.: Investigating potential biases in observed and modeled
1316 metrics of aerosol-cloud-precipitation interactions, *Atmos. Chem. Phys.*, 11, 4027-4037,
1317 10.5194/acp-11-4027-2011, 2011.

1318 Fan, C., Wang, M., Rosenfeld, D., Zhu, Y., Liu, J., and Chen, B.: Strong Precipitation Suppression by
1319 Aerosols in Marine Low Clouds, *Geophys. Res. Lett.*, 47, e2019GL086207,
1320 <https://doi.org/10.1029/2019GL086207>, 2020.

1321 Feingold, G., Frisch, A. S., Stevens, B., and Cotton, W. R.: On the relationship among cloud turbulence,
1322 droplet formation and drizzle as viewed by Doppler radar, microwave radiometer and lidar, *J.*
1323 *Geophys. Res.-Atmos.*, 104, 22195-22203, <https://doi.org/10.1029/1999JD900482>, 1999.

1324 Feingold, G., Kreidenweis, S. M., Stevens, B., and Cotton, W. R.: Numerical simulations of
1325 stratocumulus processing of cloud condensation nuclei through collision-coalescence, *J. Geophys.*
1326 *Res.-Atmos.*, 101, 21391-21402, <https://doi.org/10.1029/96JD01552>, 1996.

1327 Feingold, G. and McComiskey, A.: ARM's Aerosol-Cloud-Precipitation Research (Aerosol Indirect Effects),
1328 *Meteor. Monogr.*, 57, 22.21-22.15, 10.1175/AMSMONOGRAPHS-D-15-0022.1, 2016.

1329 Feingold, G. and Siebert, H.: Cloud – Aerosol Interactions from the Micro to the Cloud Scale, from the
1330 Strungmann Forum Report, *Clouds in the Perturbed Climate System: Their Relationship to Energy*
1331 *Balance, Atmospheric Dynamics, and Precipitation*, 2, edited by: Heintzenberg, J. and Charlson, R.
1332 J., MIT Press, ISBN 978-0-262-01287-4, 2009.

1333 Flossmann, A. I., Hall, W. D., and Pruppacher, H. R.: A Theoretical Study of the Wet Removal of
1334 Atmospheric Pollutants. Part I: The Redistribution of Aerosol Particles Captured through
1335 Nucleation and Impaction Scavenging by Growing Cloud Drops, *J. Atmos. Sci.*, 42, 583-606,
1336 [https://doi.org/10.1175/1520-0469\(1985\)042<0583:ATSOTW>2.0.CO;2](https://doi.org/10.1175/1520-0469(1985)042<0583:ATSOTW>2.0.CO;2), 1985.

1337 Gao, S., Lu, C., Liu, Y., Mei, F., Wang, J., Zhu, L., and Yan, S.: Contrasting Scale Dependence of
1338 Entrainment-Mixing Mechanisms in Stratocumulus Clouds, *Geophys. Res. Lett.*, 47,
1339 e2020GL086970, <https://doi.org/10.1029/2020GL086970>, 2020.

1340 Ghate, V. P. and Cadetdu, M. P.: Drizzle and Turbulence Below Closed Cellular Marine Stratocumulus
1341 Clouds, *J. Geophys. Res.-Atmos.*, 124, 5724-5737, <https://doi.org/10.1029/2018JD030141>, 2019.

1342 Ghate, V. P., Cadetdu, M. P., Zheng, X., and O'Connor, E.: Turbulence in the Marine Boundary Layer
1343 and Air Motions below Stratocumulus Clouds at the ARM Eastern North Atlantic Site, *J. Appl.*
1344 *Meteorol. Clim.*, 60, 1495-1510, 10.1175/JAMC-D-21-0087.1, 2021.

1345 Grabowski, W. W. and Wang, L.-P.: Growth of Cloud Droplets in a Turbulent Environment, *Annual*
1346 *Review of Fluid Mechanics*, 45, 293-324, 10.1146/annurev-fluid-011212-140750, 2013.

1347 Grosvenor, D. P., Sourdeval, O., Zuidema, P., Ackerman, A., Alexandrov, M. D., Bennartz, R., Boers,
1348 R., Cairns, B., Chiu, J. C., Christensen, M., Deneke, H., Diamond, M., Feingold, G., Fridlind, A.,
1349 Hünerbein, A., Knist, C., Kollias, P., Marshak, A., McCoy, D., Merk, D., Painemal, D., Rausch, J.,
1350 Rosenfeld, D., Russchenberg, H., Seifert, P., Sinclair, K., Stier, P., van Diedenhoven, B., Wendisch,
1351 M., Werner, F., Wood, R., Zhang, Z., and Quaas, J.: Remote Sensing of Droplet Number
1352 Concentration in Warm Clouds: A Review of the Current State of Knowledge and Perspectives,
1353 *Reviews of Geophysics*, 56, 409-453, <https://doi.org/10.1029/2017RG000593>, 2018.

1354 Gupta, S., McFarquhar, G. M., O'Brien, J. R., Delene, D. J., Poellot, M. R., Dobracki, A., Podolske, J.
1355 R., Redemann, J., LeBlanc, S. E., Segal-Rozenhaimer, M., and Pistone, K.: Impact of the variability
1356 in vertical separation between biomass burning aerosols and marine stratocumulus on cloud

1357 microphysical properties over the Southeast Atlantic, *Atmos. Chem. Phys.*, 21, 4615– 4635,
1358 <https://doi.org/10.5194/acp-21-4615-2021>, 2021.

1359 Gupta, S., McFarquhar, G. M., O'Brien, J. R., Poellot, M. R., Delene, D. J., Miller, R. M., and Small
1360 Griswold, J. D.: Factors affecting precipitation formation and precipitation susceptibility of marine
1361 stratocumulus with variable above- and below-cloud aerosol concentrations over the Southeast
1362 Atlantic, *Atmos. Chem. Phys.*, 22, 2769–2793, <https://doi.org/10.5194/acp-22-2769-2022>, 2022.

1363 Hansen, J. E. and Travis, L. D.: Light scattering in planetary atmospheres, *Space Sci. Rev.*, 16, 527-610,
1364 doi:10.1007/BF00168069,1974.

1365 Hill, A. A., Feingold, G., and Jiang, H.: The Influence of Entrainment and Mixing Assumption on
1366 Aerosol–Cloud Interactions in Marine Stratocumulus, *J. Atmos. Sci.*, 66, 1450-1464,
1367 [10.1175/2008JAS2909.1](https://doi.org/10.1175/2008JAS2909.1), 2009.

1368 Hinds, W.C.: *Aerosol Technology, Properties, Behaviour, and Measurement of Airborne Particles*. John
1369 Wiley & Sons Inc., New York., 1999.

1370 Hoffmann, F. and Feingold, G.: A Note on Aerosol Processing by Droplet Collision-Coalescence,
1371 *Geophys. Res. Lett.*, 50, e2023GL103716, <https://doi.org/10.1029/2023GL103716>, 2023.

1372 Hu, A. Z., Igel, A. L., Chuang, P. Y., and Witte, M. K.: Recognition of Inter-Cloud Versus Intra-Cloud
1373 Controls on Droplet Dispersion With Applications to Microphysics Parameterization, *J. Geophys.*
1374 *Res.-Atmos.*, 126, e2021JD035180, <https://doi.org/10.1029/2021JD035180>, 2021.

1375 Hudson, J. G. and Noble, S.: CCN Spectral Shape and Cumulus Cloud and Drizzle Microphysics, *J.*
1376 *Geophys. Res.-Atmos.*, 125, e2019JD031141, <https://doi.org/10.1029/2019JD031141>, 2020.

1377 Jensen, M. P., Ghate, V. P., Wang, D., Apoznanski, D. K., Bartholomew, M. J., Giangrande, S. E.,
1378 Johnson, K. L., and Thieman, M. M.: Contrasting characteristics of open- and closed-cellular
1379 stratocumulus cloud in the eastern North Atlantic, *Atmos. Chem. Phys.*, 21, 14557-14571,
1380 [10.5194/acp-21-14557-2021](https://doi.org/10.5194/acp-21-14557-2021), 2021.

1381 Jones, C. R., Bretherton, C. S., and Leon, D.: Coupled vs. decoupled boundary layers in VOCALS-REx,
1382 Atmos. Chem. Phys., 11, 7143-7153, 10.5194/acp-11-7143-2011, 2011.

1383 Jung, E., Albrecht, B. A., Sorooshian, A., Zuidema, P., and Jonsson, H. H.: Precipitation susceptibility
1384 in marine stratocumulus and shallow cumulus from airborne measurements, Atmos. Chem. Phys.,
1385 16, 11395-11413, 10.5194/acp-16-11395-2016, 2016.

1386 Kang, L., Marchand, R. T., Wood, R., and McCoy, I. L.: Coalescence Scavenging Drives Droplet
1387 Number Concentration in Southern Ocean Low Clouds, Geophys. Res. Lett., 49, e2022GL097819,
1388 <https://doi.org/10.1029/2022GL097819>, 2022.

1389 Kang, L., Marchand, R. T., and Wood, R.: Stratocumulus Precipitation Properties Over the Southern
1390 Ocean Observed From Aircraft During the SOCRATES Campaign, J. Geophys. Res.-Atmos., 129,
1391 e2023JD039831, <https://doi.org/10.1029/2023JD039831>, 2024.

1392 Kim, S. H., Kim, J., Kim, J. H., and Chun, H. Y.: Characteristics of the derived energy dissipation rate
1393 using the 1 Hz commercial aircraft quick access recorder (QAR) data, Atmos. Meas. Tech.,
1394 15, 2277-2298, 10.5194/amt-15-2277-2022, 2022.

1395 Lang, F., Ackermann, L., Huang, Y., Truong, S. C. H., Siems, S. T., and Manton, M. J.: A climatology
1396 of open and closed mesoscale cellular convection over the Southern Ocean derived from Himawari-
1397 8 observations, Atmos. Chem. Phys., 22, 2135-2152, 10.5194/acp-22-2135-2022, 2022.

1398 Lu, C., Zhu, L., Liu, Y., Mei, F., Fast, J. D., Pekour, M. S., Luo, S., Xu, X., He, X., Li, J., and Gao, S.:
1399 Observational study of relationships between entrainment rate, homogeneity of mixing, and cloud
1400 droplet relative dispersion, Atmos. Res., 293, 106900,
1401 <https://doi.org/10.1016/j.atmosres.2023.106900>, 2023.

1402 Lu, M.-L., Sorooshian, A., Jonsson, H. H., Feingold, G., Flagan, R. C., and Seinfeld, J. H.: Marine
1403 stratocumulus aerosol-cloud relationships in the MASE-II experiment: Precipitation susceptibility
1404 in eastern Pacific marine stratocumulus, J. Geophys. Res.-Atmos., 114,
1405 <https://doi.org/10.1029/2009JD012774>, 2009.

1406 Mann, J. A. L., Christine Chiu, J., Hogan, R. J., O'Connor, E. J., L'Ecuyer, T. S., Stein, T. H. M., and
1407 Jefferson, A.: Aerosol impacts on drizzle properties in warm clouds from ARM Mobile Facility
1408 maritime and continental deployments, *J. Geophys. Res.-Atmos.*, 119, 4136-4148,
1409 <https://doi.org/10.1002/2013JD021339>, 2014.

1410 Marcovecchio, A. R., Xi, B., Zheng, X., Wu, P., Dong, X., and Behrangi, A.: What Are the Similarities
1411 and Differences in Marine Boundary Layer Cloud and Drizzle Microphysical Properties During the
1412 ACE-ENA and MARCUS Field Campaigns?, *J. Geophys. Res.-Atmos.*, 128, e2022JD037109,
1413 <https://doi.org/10.1029/2022JD037109>, 2023.

1414 Mechem, D. B., Wittman, C. S., Miller, M. A., Yuter, S. E., and de Szoeke, S. P.: Joint Synoptic and
1415 Cloud Variability over the Northeast Atlantic near the Azores, *J. Appl. Meteorol. Clim.*, 57, 1273-
1416 1290, <https://doi.org/10.1175/JAMC-D-17-0211.1>, 2018.

1417 McComiskey, A., Feingold, G., Frisch, A. S., Turner, D. D., Miller, M. A., Chiu, J. C., Min, Q., and
1418 Ogren, J. A.: An assessment of aerosol-cloud interactions in marine stratus clouds based on surface
1419 remote sensing, *J. Geophys. Res.-Atmos.*, 114, <https://doi.org/10.1029/2008JD011006>, 2009.

1420 McCoy, I. L., Wood, R., and Fletcher, J. K.: Identifying Meteorological Controls on Open and Closed
1421 Mesoscale Cellular Convection Associated with Marine Cold Air Outbreaks, *J. Geophys. Res.-*
1422 *Atmos.*, 122, 11,678-611,702, <https://doi.org/10.1002/2017JD027031>, 2017.

1423 McCoy, I. L., McCoy, D. T., Wood, R., Regayre, L., Watson-Parris, D., Grosvenor, D. P., Mulcahy, J.
1424 P., Hu, Y., Bender, F. A. M., Field, P. R., Carslaw, K. S., and Gordon, H.: The hemispheric contrast
1425 in cloud microphysical properties constrains aerosol forcing, *P. Natl. Acad. Sci. USA*, 117, 18998-
1426 19006, [10.1073/pnas.1922502117](https://doi.org/10.1073/pnas.1922502117), 2020.

1427 McCoy, I. L., Bretherton, C. S., Wood, R., Twohy, C. H., Gettelman, A., Bardeen, C. G., and Toohey,
1428 D. W.: Influences of Recent Particle Formation on Southern Ocean Aerosol Variability and Low
1429 Cloud Properties, *J. Geophys. Res.-Atmos.*, 126, e2020JD033529,
1430 <https://doi.org/10.1029/2020JD033529>, 2021.

1431 McFarquhar, G. M., Bretherton, C. S., Marchand, R., Protat, A., DeMott, P. J., Alexander, S. P., Roberts,
1432 G. C., Twohy, C. H., Toohey, D., Siems, S., Huang, Y., Wood, R., Rauber, R. M., Lasher-Trapp,
1433 S., Jensen, J., Stith, J. L., Mace, J., Um, J., Järvinen, E., Schnaiter, M., Gettelman, A., Sanchez, K.
1434 J., McCluskey, C. S., Russell, L. M., McCoy, I. L., Atlas, R. L., Bardeen, C. G., Moore, K. A., Hill,
1435 T. C. J., Humphries, R. S., Keywood, M. D., Ristovski, Z., Cravigan, L., Schofield, R., Fairall, C.,
1436 Mallet, M. D., Kreidenweis, S. M., Rainwater, B., D'Alessandro, J., Wang, Y., Wu, W., Saliba, G.,
1437 Levin, E. J. T., Ding, S., Lang, F., Truong, S. C. H., Wolff, C., Haggerty, J., Harvey, M. J.,
1438 Klekociuk, A. R., and McDonald, A.: Observations of Clouds, Aerosols, Precipitation, and Surface
1439 Radiation over the Southern Ocean: An Overview of CAPRICORN, MARCUS, MICRE, and
1440 SOCRATES, *B. Am. Meteorol. Soc.*, 102, E894-E928, [https://doi.org/10.1175/BAMS-D-20-](https://doi.org/10.1175/BAMS-D-20-0132.1)
1441 0132.1, 2021.

1442 Muñoz-Esparza, D., Sharman, R. D., and Lundquist, J. K.: Turbulence Dissipation Rate in the
1443 Atmospheric Boundary Layer: Observations and WRF Mesoscale Modeling during the XPIA Field
1444 Campaign, *Mon. Weather Rev.*, 146, 351-371, <https://doi.org/10.1175/MWR-D-17-0186.1>, 2018.

1445 Olfert, J. S., Kulkarni, P., and Wang, J.: Measuring aerosol size distributions with the fast integrated
1446 mobility spectrometer, *Journal of Aerosol Science*, 39, 940-956,
1447 <https://doi.org/10.1016/j.jaerosci.2008.06.005>, 2008.

1448 Painemal, D. and Zuidema, P.: Assessment of MODIS cloud effective radius and optical thickness
1449 retrievals over the Southeast Pacific with VOCALS-REx in situ measurements, *J. Geophys. Res.-*
1450 *Atmos.*, 116, <https://doi.org/10.1029/2011JD016155>, 2011.

1451 Painemal, D., Chang, F. L., Ferrare, R., Burton, S., Li, Z., Smith Jr, W. L., Minnis, P., Feng, Y., and
1452 Clayton, M.: Reducing uncertainties in satellite estimates of aerosol–cloud interactions over the
1453 subtropical ocean by integrating vertically resolved aerosol observations, *Atmos. Chem. Phys.*, 20,
1454 7167-7177, [10.5194/acp-20-7167-2020](https://doi.org/10.5194/acp-20-7167-2020), 2020.

1455 Painemal, D., Spangenberg, D., Smith Jr, W. L., Minnis, P., Cairns, B., Moore, R. H., Crosbie, E.,
1456 Robinson, C., Thornhill, K. L., Winstead, E. L., and Ziemba, L.: Evaluation of satellite retrievals of
1457 liquid clouds from the GOES-13 imager and MODIS over the midlatitude North Atlantic during the
1458 NAAMES campaign, *Atmos. Meas. Tech.*, 14, 6633-6646, 10.5194/amt-14-6633-2021, 2021.

1459 Pinsky, M. B. and Khain, A. P.: Turbulence effects on droplet growth and size distribution in clouds—
1460 A review, *Journal of Aerosol Science*, 28, 1177-1214, [https://doi.org/10.1016/S0021-](https://doi.org/10.1016/S0021-8502(97)00005-0)
1461 [8502\(97\)00005-0](https://doi.org/10.1016/S0021-8502(97)00005-0), 1997.

1462 Pruppacher, H. R. and Klett, J. D.: *Microphysics of clouds and precipitation*, Kluwer Academic
1463 Publishers, Dordrecht, the Netherlands, 1997.

1464 [Redemann, J., Wood, R., Zuidema, P., Doherty, S. J., Luna, B., LeBlanc, S. E., Diamond, M. S.,](#)
1465 [Shinozuka, Y., Chang, I. Y., Ueyama, R., Pfister, L., Ryoo, J. M., Dobracki, A. N., da Silva, A. M.,](#)
1466 [Longo, K. M., Kacenelenbogen, M. S., Flynn, C. J., Pistone, K., Knox, N. M., Piketh, S. J.,](#)
1467 [Haywood, J. M., Formenti, P., Mallet, M., Stier, P., Ackerman, A. S., Bauer, S. E., Fridlind, A. M.,](#)
1468 [Carmichael, G. R., Saide, P. E., Ferrada, G. A., Howell, S. G., Freitag, S., Cairns, B., Holben, B.](#)
1469 [N., Knobelspiesse, K. D., Tanelli, S., L'Ecuyer, T. S., Dzambo, A. M., Sy, O. O., McFarquhar, G.](#)
1470 [M., Poellot, M. R., Gupta, S., O'Brien, J. R., Nenes, A., Kacarab, M., Wong, J. P. S., Small-](#)
1471 [Griswold, J. D., Thornhill, K. L., Noone, D., Podolske, J. R., Schmidt, K. S., Pilewskie, P., Chen,](#)
1472 [H., Cochrane, S. P., Sedlacek, A. J., Lang, T. J., Stith, E., Segal-Rozenhaimer, M., Ferrare, R. A.,](#)
1473 [Burton, S. P., Hostetler, C. A., Diner, D. J., Seidel, F. C., Platnick, S. E., Myers, J. S., Meyer, K. G.,](#)
1474 [Spangenberg, D. A., Maring, H., and Gao, L.: An overview of the ORACLES \(ObseRvations of](#)
1475 [Aerosols above CLOUDs and their intERactionS\) project: aerosol–cloud–radiation interactions in the](#)
1476 [southeast Atlantic basin, *Atmos. Chem. Phys.*, 21, 1507-1563, 10.5194/acp-21-1507-2021, 2021.](#)

1477 Rémillard, J. and Tselioudis, G.: Cloud Regime Variability over the Azores and Its Application to
1478 Climate Model Evaluation, *J. Climate*, 28, 9707-9720, <https://doi.org/10.1175/JCLI-D-15-0066.1>,
1479 2015.

1480 Sanchez, K. J., Roberts, G. C., Diao, M., and Russell, L. M.: Measured Constraints on Cloud Top
1481 Entrainment to Reduce Uncertainty of Nonprecipitating Stratocumulus Shortwave Radiative
1482 Forcing in the Southern Ocean, *Geophys. Res. Lett.*, 47, e2020GL090513,
1483 <https://doi.org/10.1029/2020GL090513>, 2020.

1484 Sanchez, K. J., Roberts, G. C., Saliba, G., Russell, L. M., Twohy, C., Reeves, J. M., Humphries, R. S.,
1485 Keywood, M. D., Ward, J. P., and McRobert, I. M.: Measurement report: Cloud processes and the
1486 transport of biological emissions affect southern ocean particle and cloud condensation nuclei
1487 concentrations, *Atmos. Chem. Phys.*, 21, 3427-3446, 10.5194/acp-21-3427-2021, 2021.

1488 Siebert, H., Shaw, R. A., and Warhaft, Z.: Statistics of Small-Scale Velocity Fluctuations and Internal
1489 Intermittency in Marine Stratocumulus Clouds, *J. Atmos. Sci.*, 67, 262-273,
1490 <https://doi.org/10.1175/2009JAS3200.1>, 2010.

1491 Smalley, M. A., Witte, M. K., Jeong, J.-H., and Chinita, M. J.: A climatology of cold pools distinct from
1492 background turbulence at the Eastern North Atlantic observations site, *EGUsphere* [preprint],
1493 <https://doi.org/10.5194/egusphere-2024-1098>, 2024.

1494 Stevens, B. and Feingold, G.: Untangling aerosol effects on clouds and precipitation in a buffered system,
1495 *Nature*, 461, 607-613, 10.1038/nature08281, 2009.

1496 Sorooshian, A., Feingold, G., Lebsock, M. D., Jiang, H., and Stephens, G. L.: On the precipitation
1497 susceptibility of clouds to aerosol perturbations, *Geophys. Res. Lett.*, 36,
1498 <https://doi.org/10.1029/2009GL038993>, 2009.

1499 [Sorooshian, A., Anderson, B., Bauer, S. E., Braun, R. A., Cairns, B., Crosbie, E., Dadashazar, H., Diskin,](#)
1500 [G., Ferrare, R., Flagan, R. C., Hair, J., Hostetler, C., Jonsson, H. H., Kleb, M. M., Liu, H.,](#)
1501 [MacDonald, A. B., McComiskey, A., Moore, R., Painemal, D., Russell, L. M., Seinfeld, J. H.,](#)
1502 [Shook, M., Smith, W. L., Thornhill, K., Tselioudis, G., Wang, H., Zeng, X., Zhang, B., Ziemba, L.,](#)
1503 [and Zuidema, P.: Aerosol–Cloud–Meteorology Interaction Airborne Field Investigations: Using](#)

1504 [Lessons Learned from the U.S. West Coast in the Design of ACTIVATE off the U.S. East Coast,](#)
1505 [B. Am. Meteorol. Soc., 100, 1511-1528, <https://doi.org/10.1175/BAMS-D-18-0100.1>, 2019.](#)

1506 Su, T., Li, Z., Henao, N. R., Luan, Q., and Yu, F.: Constraining effects of aerosol-cloud interaction by
1507 accounting for coupling between cloud and land surface, *Science Advances*, 10, ead15044,
1508 [10.1126/sciadv.ad15044](https://doi.org/10.1126/sciadv.ad15044),

1509 Terai, C. R. and Wood, R.: Aircraft observations of cold pools under marine stratocumulus, *Atmos.*
1510 *Chem. Phys.*, 13, 9899-9914, [10.5194/acp-13-9899-2013](https://doi.org/10.5194/acp-13-9899-2013), 2013.

1511 Terai, C. R., Wood, R., Leon, D. C., and Zuidema, P.: Does precipitation susceptibility vary with
1512 increasing cloud thickness in marine stratocumulus?, *Atmos. Chem. Phys.*, 12, 4567-4583,
1513 [10.5194/acp-12-4567-2012](https://doi.org/10.5194/acp-12-4567-2012), 2012.

1514 Twohy, C. H., Petters, M. D., Snider, J. R., Stevens, B., Tahnk, W., Wetzal, M., Russell, L., and Burnet,
1515 F.: Evaluation of the aerosol indirect effect in marine stratocumulus clouds: Droplet number, size,
1516 liquid water path, and radiative impact, *J. Geophys. Res.-Atmos.*, 110,
1517 <https://doi.org/10.1029/2004JD005116>, 2005.

1518 vanZanten, M. C., Stevens, B., Vali, G., and Lenschow, D. H.: Observations of Drizzle in Nocturnal
1519 Marine Stratocumulus, *J. Atmos. Sci.*, 62, 88-106, <https://doi.org/10.1175/JAS-3355.1>, 2005.

1520 Waclawczyk, M., Ma, Y. F., Kopeć, J. M., and Malinowski, S. P.: Novel approaches to estimating the
1521 turbulent kinetic energy dissipation rate from low- and moderate-resolution velocity fluctuation
1522 time series, *Atmos. Meas. Tech.*, 10, 4573-4585, [10.5194/amt-10-4573-2017](https://doi.org/10.5194/amt-10-4573-2017), 2017.

1523 Wang, J., Wood, R., Jensen, M. P., Chiu, J. C., Liu, Y., Lamer, K., Desai, N., Giangrande, S. E., Knopf,
1524 D. A., Kollias, P., Laskin, A., Liu, X., Lu, C., Mechem, D., Mei, F., Starzec, M., Tomlinson, J.,
1525 Wang, Y., Yum, S. S., Zheng, G., Aiken, A. C., Azevedo, E. B., Blanchard, Y., China, S., Dong,
1526 X., Gallo, F., Gao, S., Ghate, V. P., Glienke, S., Goldberger, L., Hardin, J. C., Kuang, C., Luke, E.
1527 P., Matthews, A. A., Miller, M. A., Moffet, R., Pekour, M., Schmid, B., Sedlacek, A. J., Shaw, R.
1528 A., Shilling, J. E., Sullivan, A., Suski, K., Veghte, D. P., Weber, R., Wyant, M., Yeom, J.,

1529 Zawadowicz, M., and Zhang, Z.: Aerosol and Cloud Experiments in the Eastern North Atlantic
1530 (ACE-ENA), *B. Am. Meteorol. Soc.*, 103, E619-E641, 10.1175/BAMS-D-19-0220.1, 2022.

1531 Wang, Y., Zhao, C., McFarquhar, G. M., Wu, W., Reeves, M., and Li, J.: Dispersion of Droplet Size
1532 Distributions in Supercooled Non-precipitating Stratocumulus from Aircraft Observations Obtained
1533 during the Southern Ocean Cloud Radiation Aerosol Transport Experimental Study, *J. Geophys.*
1534 *Res.-Atmos.*, 126, e2020JD033720, <https://doi.org/10.1029/2020JD033720>, 2021a.

1535 Wang, Y., Zheng, G., Jensen, M. P., Knopf, D. A., Laskin, A., Matthews, A. A., Mechem, D., Mei, F.,
1536 Moffet, R., Sedlacek, A. J., Shilling, J. E., Springston, S., Sullivan, A., Tomlinson, J., Veghte, D.,
1537 Weber, R., Wood, R., Zawadowicz, M. A., and Wang, J.: Vertical profiles of trace gas and aerosol
1538 properties over the eastern North Atlantic: variations with season and synoptic condition, *Atmos.*
1539 *Chem. Phys.*, 21, 11079-11098, 10.5194/acp-21-11079-2021, 2021b.

1540 Wang, Y., Zheng, X., Dong, X., Xi, B., Wu, P., Logan, T., and Yung, Y. L.: Impacts of long-range
1541 transport of aerosols on marine-boundary-layer clouds in the eastern North Atlantic, *Atmos. Chem.*
1542 *Phys.*, 20, 14741-14755, 10.5194/acp-20-14741-2020, 2020.

1543 Wang, Y., Zheng, X., Dong, X., Xi, B., and Yung, Y. L.: Insights of warm-cloud biases in Community
1544 Atmospheric Model 5 and 6 from the single-column modeling framework and Aerosol and Cloud
1545 Experiments in the Eastern North Atlantic (ACE-ENA) observations, *Atmos. Chem. Phys.*, 23,
1546 8591-8605, 10.5194/acp-23-8591-2023, 2023.

1547 Wallace, J. M. and Hobbs, P. V.: *Atmospheric Science: An Introductory Survey*, 2nd edn., Academic
1548 Press/Elsevier, 483 pp, 2006.

1549 Witte, M. K., Chuang, P. Y., Ayala, O., Wang, L.-P., and Feingold, G.: Comparison of Observed and
1550 Simulated Drop Size Distributions from Large-Eddy Simulations with Bin Microphysics, *Mon.*
1551 *Weather Rev.*, 147, 477-493, <https://doi.org/10.1175/MWR-D-18-0242.1>, 2019.

1552 Wood, R.: Drizzle in Stratiform Boundary Layer Clouds. Part I: Vertical and Horizontal Structure, *J.*
1553 *Atmos. Sci.*, 62, 3011-3033, 10.1175/JAS3529.1, 2005.

1554 Wood, R.: Rate of loss of cloud droplets by coalescence in warm clouds, *J. Geophys. Res.-Atmos.*, 111,
1555 <https://doi.org/10.1029/2006JD007553>, 2006.

1556 Wood, R., [Mechozo, C. R.](#), [Bretherton, C. S.](#), [Weller, R. A.](#), [Huebert, B.](#), [Straneo, F.](#), [Albrecht, B. A.](#),
1557 [Coe, H.](#), [Allen, G.](#), [Vaughan, G.](#), [Daum, P.](#), [Fairall, C.](#), [Chand, D.](#), [Gallardo Klenner, L.](#), [Garreaud,](#)
1558 [R.](#), [Grados, C.](#), [Covert, D. S.](#), [Bates, T. S.](#), [Krejci, R.](#), [Russell, L. M.](#), [de Szoeke, S.](#), [Brewer, A.](#),
1559 [Yuter, S. E.](#), [Springston, S. R.](#), [Chaigneau, A.](#), [Toniazzi, T.](#), [Minnis, P.](#), [Palikonda, R.](#), [Abel, S. J.](#),
1560 [Brown, W. O. J.](#), [Williams, S.](#), [Fochesatto, J.](#), [Brioude, J.](#), and [Bower, K. N.](#): *The VAMOS Ocean-*
1561 *Cloud-Atmosphere-Land Study Regional Experiment (VOCALS-REx): goals, platforms, and field*
1562 *operations, Atmos. Chem. Phys.*, 11, 627-654, [10.5194/acp-11-627-2011](https://doi.org/10.5194/acp-11-627-2011), 2011.

1563 [Wood, R.](#), Wyant, M., Bretherton, C. S., Rémillard, J., Kollias, P., Fletcher, J., Stemmler, J., de Szoeke,
1564 S., Yuter, S., Miller, M., Mechem, D., Tselioudis, G., Chiu, J. C., Mann, J. A. L., O'Connor, E. J.,
1565 Hogan, R. J., Dong, X., Miller, M., Ghate, V., Jefferson, A., Min, Q., Minnis, P., Palikonda, R.,
1566 Albrecht, B., Luke, E., Hannay, C., and Lin, Y.: Clouds, Aerosols, and Precipitation in the Marine
1567 Boundary Layer: An Arm Mobile Facility Deployment, *B. Am. Meteorol. Soc.*, 96, 419-440,
1568 [10.1175/BAMS-D-13-00180.1](https://doi.org/10.1175/BAMS-D-13-00180.1), 2015.

1569 Wu, P., Dong, X., and Xi, B.: A Climatology of Marine Boundary Layer Cloud and Drizzle Properties
1570 Derived from Ground-Based Observations over the Azores, *J. Climate*, 33, 10133-10148,
1571 [10.1175/JCLI-D-20-0272.1](https://doi.org/10.1175/JCLI-D-20-0272.1), 2020.

1572 Wu, P., Dong, X., Xi, B., Liu, Y., Thieman, M., and Minnis, P.: Effects of environment forcing on marine
1573 boundary layer cloud-drizzle processes, *J. Geophys. Res.-Atmos.*, 122, 4463-4478,
1574 <https://doi.org/10.1002/2016JD026326>, 2017.

1575 Wyant, M. C., Bretherton, C. S., Wood, R., Blossey, P. N., and McCoy, I. L.: High Free-Tropospheric
1576 Aitken-Mode Aerosol Concentrations Buffer Cloud Droplet Concentrations in Large-Eddy
1577 Simulations of Precipitating Stratocumulus, *Journal of Advances in Modeling Earth Systems*, 14,
1578 e2021MS002930, <https://doi.org/10.1029/2021MS002930>, 2022.

1579 Yeom, J. M., Yum, S. S., Shaw, R. A., La, I., Wang, J., Lu, C., Liu, Y., Mei, F., Schmid, B., and
1580 Matthews, A.: Vertical Variations of Cloud Microphysical Relationships in Marine Stratocumulus
1581 Clouds Observed During the ACE-ENA Campaign, *J. Geophys. Res.-Atmos.*, 126,
1582 e2021JD034700, <https://doi.org/10.1029/2021JD034700>, 2021.

1583 Zawadowicz, M. A., Suski, K., Liu, J., Pekour, M., Fast, J., Mei, F., Sedlacek, A. J., Springston, S.,
1584 Wang, Y., Zaveri, R. A., Wood, R., Wang, J., and Shilling, J. E.: Aircraft measurements of aerosol
1585 and trace gas chemistry in the eastern North Atlantic, *Atmos. Chem. Phys.*, 21, 7983-8002,
1586 10.5194/acp-21-7983-2021, 2021.

1587 Zhang, J., Zhou, X., Goren, T., and Feingold, G.: Albedo susceptibility of northeastern Pacific
1588 stratocumulus: the role of covarying meteorological conditions, *Atmos. Chem. Phys.*, 22, 861-880,
1589 10.5194/acp-22-861-2022, 2022.

1590 Zhang, X., Dong, X., Xi, B., and Zheng, X.: Aerosol Properties and Their Influences on Marine Boundary
1591 Layer Cloud Condensation Nuclei over the Southern Ocean, *Atmosphere-Basel*, 14,
1592 10.3390/atmos14081246, 2023.

1593 Zheng, G., Wang, Y., Aiken, A. C., Gallo, F., Jensen, M. P., Kollias, P., Kuang, C., Luke, E., Springston,
1594 S., Uin, J., Wood, R., and Wang, J.: Marine boundary layer aerosol in the eastern North Atlantic:
1595 seasonal variations and key controlling processes, *Atmos. Chem. Phys.*, 18, 17615-17635,
1596 10.5194/acp-18-17615-2018, 2018.

1597 Zheng, G., Wang, Y., Wood, R., Jensen, M. P., Kuang, C., McCoy, I. L., Matthews, A., Mei, F.,
1598 Tomlinson, J. M., Shilling, J. E., Zawadowicz, M. A., Crosbie, E., Moore, R., Ziemba, L., Andreae,
1599 M. O., and Wang, J.: New particle formation in the remote marine boundary layer, *Nature*
1600 *Communications*, 12, 527, 10.1038/s41467-020-20773-1, 2021.

1601 Zheng, X., Dong, X., Ward, D. M., Xi, B., Wu, P., and Wang, Y.: Aerosol-Cloud-Precipitation
1602 Interactions in a Closed-cell and Non-homogenous MBL Stratocumulus Cloud, *Adv. Atmos. Sci.*,
1603 39, 2107-2123, 10.1007/s00376-022-2013-6, 2022a.

1604 Zheng, X., Xi, B., Dong, X., Wu, P., Logan, T., and Wang, Y.: Environmental effects on aerosol–cloud
1605 interaction in non-precipitating marine boundary layer (MBL) clouds over the eastern North
1606 Atlantic, *Atmos. Chem. Phys.*, 22, 335-354, 10.5194/acp-22-335-2022, 2022b.

1607 Zuidema, P., Torri, G., Muller, C., and Chandra, A.: A Survey of Precipitation-Induced Atmospheric
1608 Cold Pools over Oceans and Their Interactions with the Larger-Scale Environment, *Surveys in*
1609 *Geophysics*, 38, 1283-1305, 10.1007/s10712-017-9447-x, 2017.

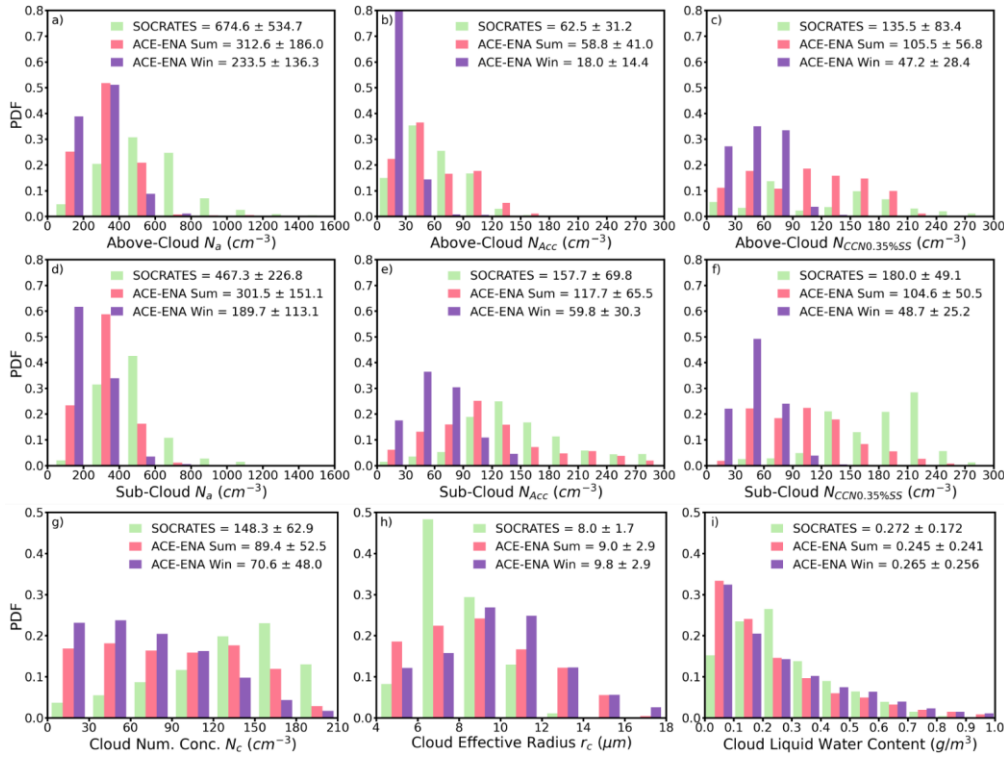


Figure 1. Probability Density Functions (PDFs) of N_a , N_{ACC} and $N_{CCN0.35\%}$ in the above-cloud (a, b, c) and sub-cloud (d, e, f) regimes; and the cloud microphysical properties of N_c (g), r_c (h), and LWC_c (f) within cloud layer. The statistical metrics in the legends denote the mean and standard deviation values for all samples in three IOPs. The ACE-ENA Sum, ACE-ENA Win, and SOCRATES are color-coded with pink, purple, and green, respectively.

Deleted: summer, winter

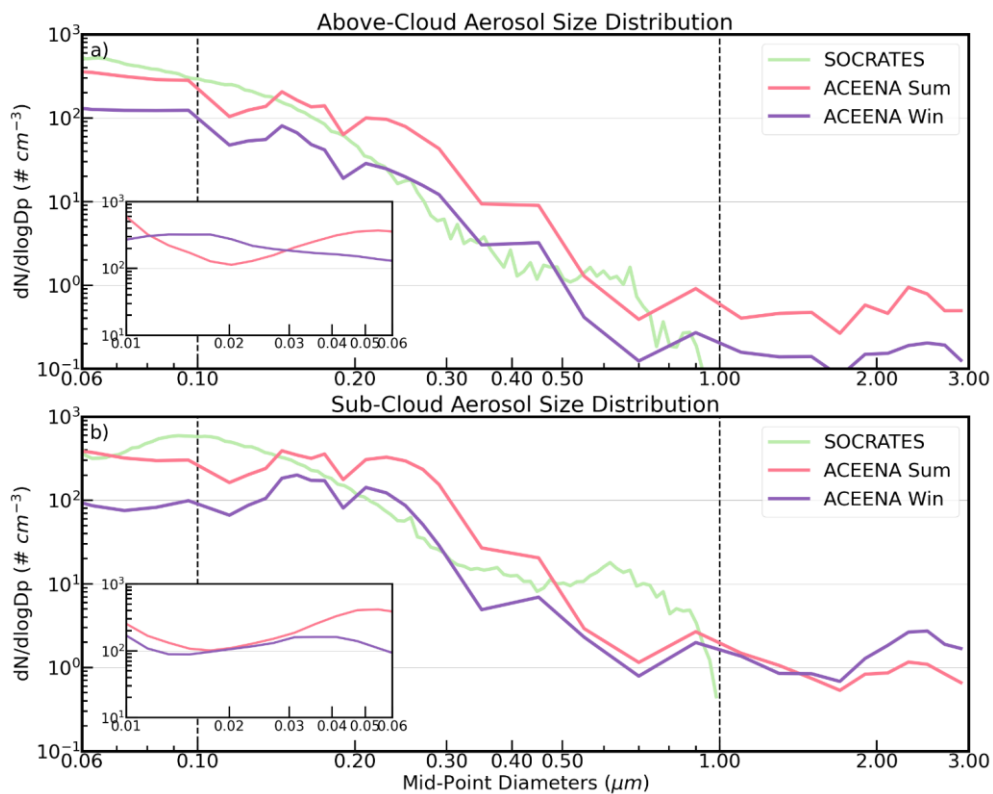


Figure 2. Aerosol size distributions ($D_p = 0.06 - 3 \mu\text{m}$) for above-cloud (a) and sub-cloud (b) regimes. The vertical dashed line at $D_p = 0.1 \mu\text{m}$ and at $D_p = 1 \mu\text{m}$ denotes the demarcations between Accumulation mode, Aitken mode and Coarse mode aerosols. The inner plots denote a smaller range of Aitken mode size distribution ($D_p = 0.01 - 0.06 \mu\text{m}$) available from ACE-ENA. The ACE-ENA Sum, ACE-ENA Win, and SOCRATES are color-coded with pink, purple, and green, respectively.

Deleted: summer, winter

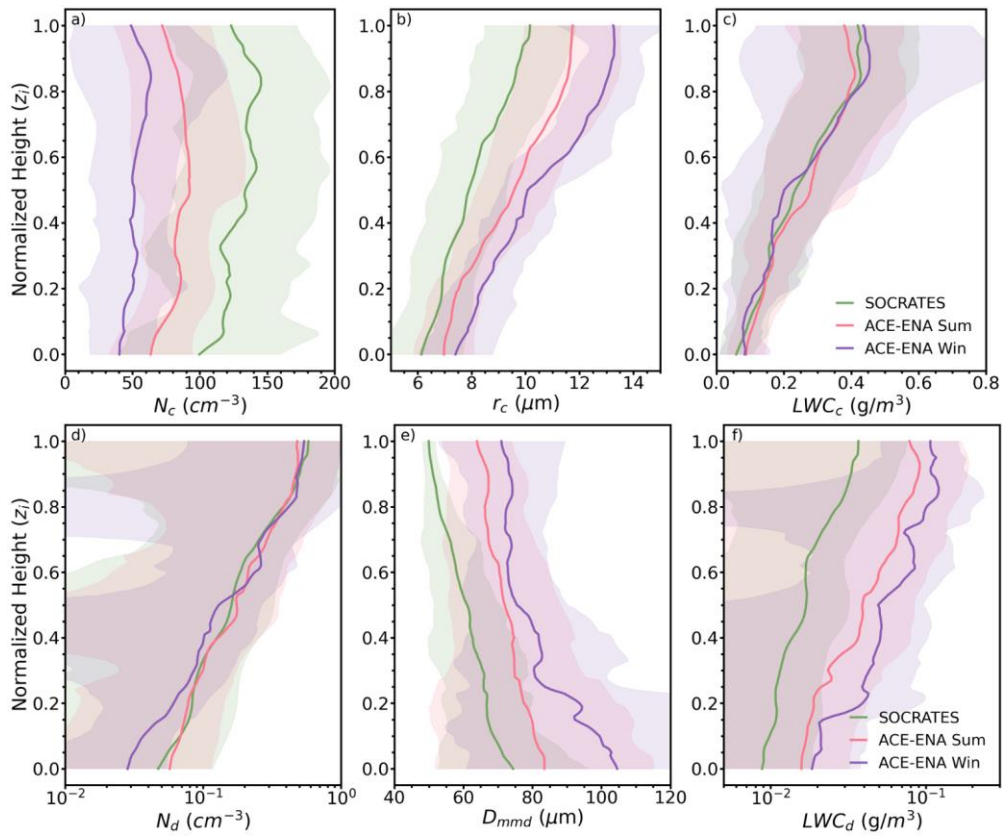
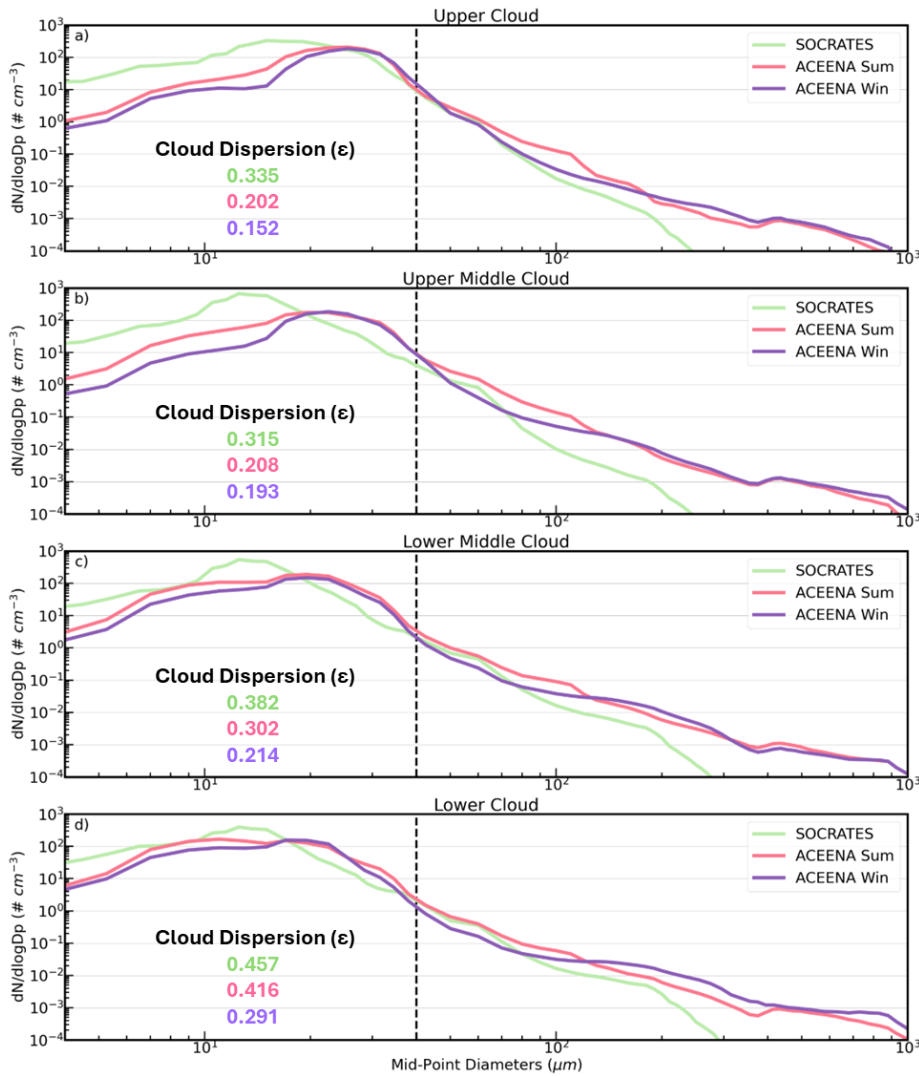


Figure 3. Vertical distributions of N_c (a), r_c (b), LWC_c (c), N_d (d), D_{mmd} (e), and LWC_d (f). Here the $z_i = 0$ denotes cloud base and $z_i = 1$ denotes cloud top. Shaded areas denote the inter-cloud-case standard deviations. The ACE-ENA ~~Sum~~, ACE-ENA Win, and SOCRATES are color-coded with pink, purple, and green, respectively.

Deleted: summer, winter



1611 **Figure 4.** Cloud and drizzle size distributions for a) upper cloud ($z_i > 0.8$), b) upper-middle cloud ($0.5 \leq$
 1612 $z_i < 0.8$), c) lower-middle cloud ($0.2 \leq z_i < 0.5$) and d) lower cloud ($z_i < 0.2$). The vertical dashed
 1613 line at $D_p = 40 \mu\text{m}$ denotes the demarcation between cloud droplets and drizzle drops. The ACE-ENA
 1614 Sum, ACE-ENA Win, and SOCRATES are color-coded with pink, purple, and green, respectively.

Deleted: summer, winter

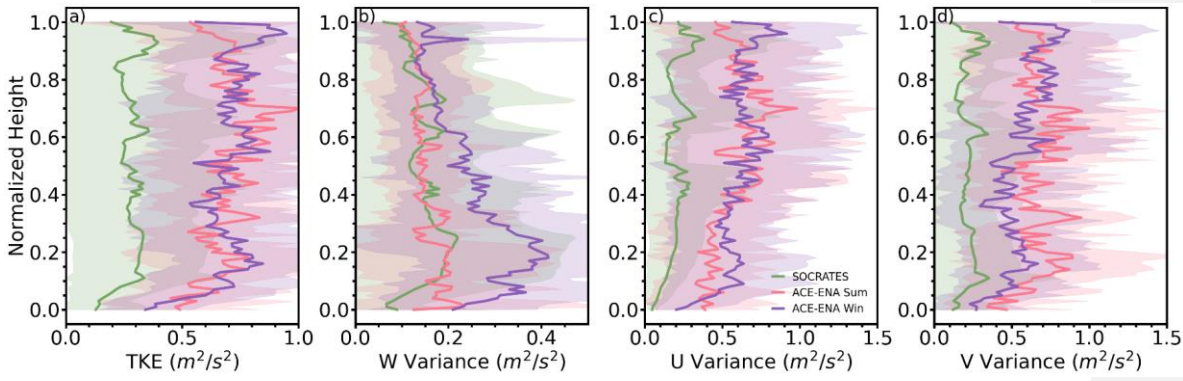


Figure 5. Vertical distributions of in-cloud TKE (a), w'^2 (b), u'^2 (c), and v'^2 (d). Shaded areas denote the inter-cloud-case standard deviations. The ACE-ENA Sum, ACE-ENA Win, and SOCRATES are color-coded with pink, purple, and green, respectively.

Deleted:)

Deleted: summer, winter

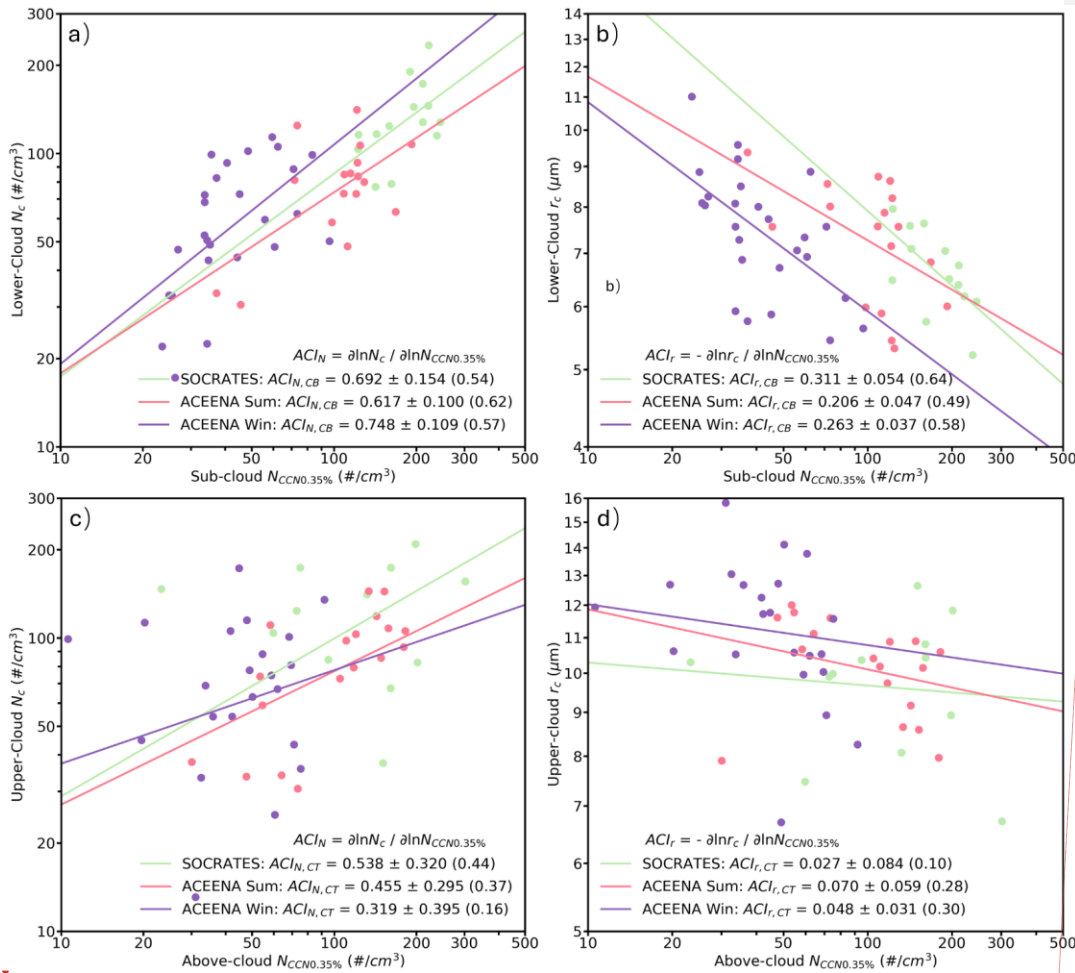
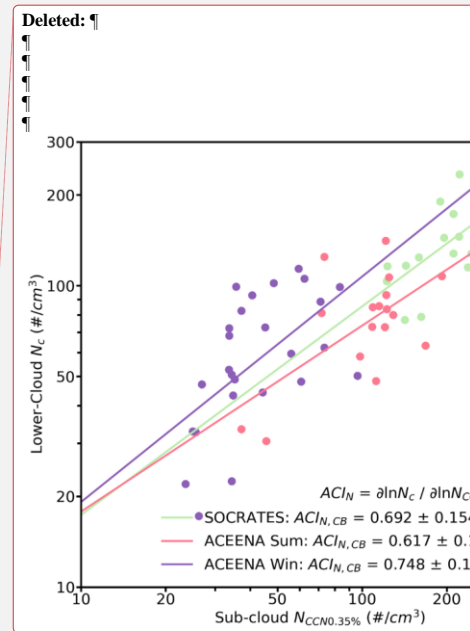


Figure 6. Scatterplots of the **a)** N_c and **b)** r_c at the lower-cloud ($z_i < 0.2$) against the sub-cloud $N_{CCN0.35\%}$ and the **c)** N_c and **d)** r_c at the upper-cloud ($z_i > 0.8$) against the above-cloud $N_{CCN0.35\%}$. The statistical metrics in the legends denote the ACI values and standard errors, and the absolute values of correlation coefficients (in parentheses). The ACE-ENA **Sum**, **ACE-ENA Win**, and **SOCRATES** are color-coded with pink, purple, and green, respectively.



Deleted: a)

Deleted: summer, winter

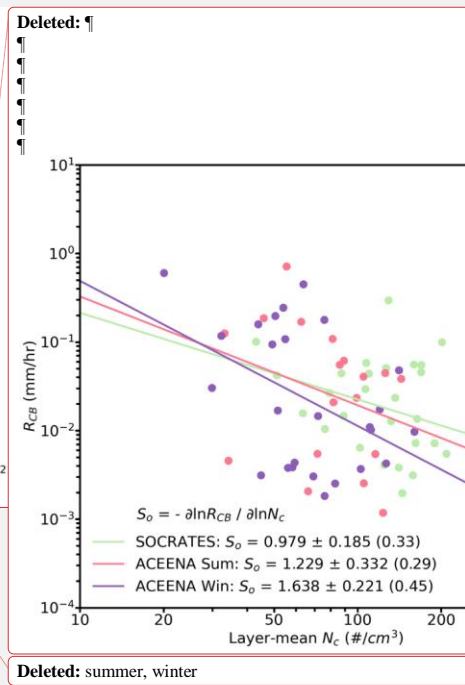
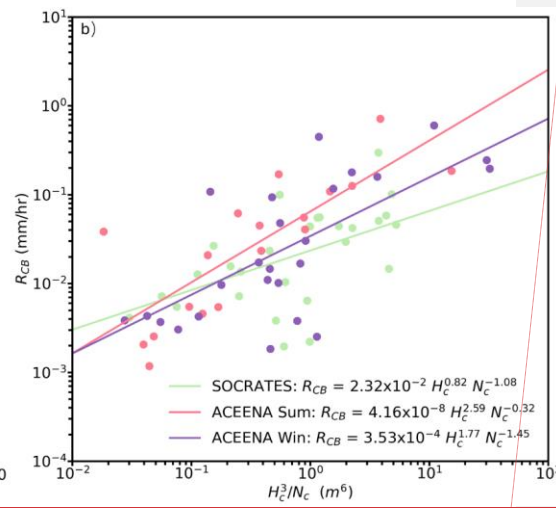
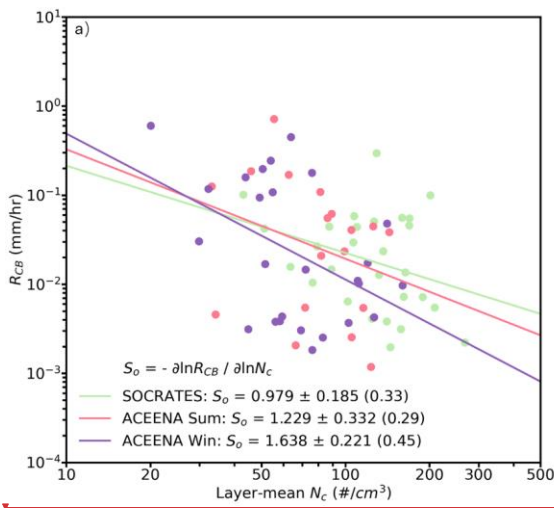


Figure 7. Scatterplots of the cloud base precipitation rate R_{CB} against the a) layer-mean N_c and b) H_c^3/N_c . The ACE-ENA Sum, ACE-ENA Win, and SOCRATES are color-coded with pink, purple, and green, respectively.

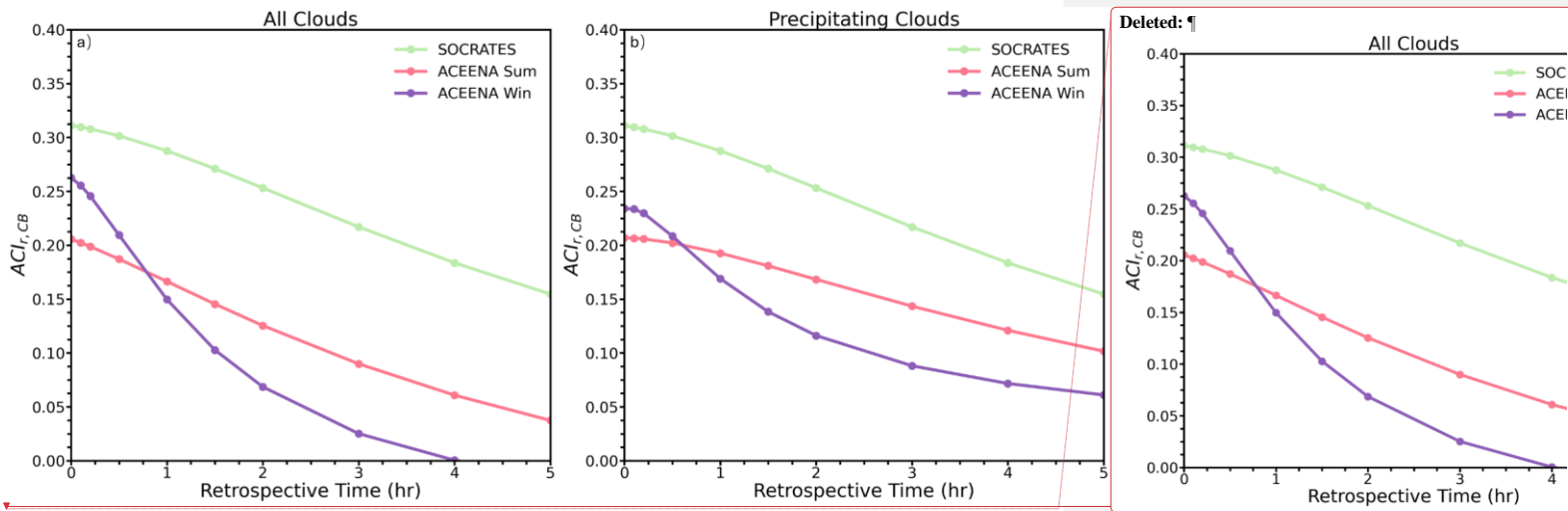


Figure 8. $ACI_{r,CB}$ as a function of the sub-cloud $N_{CCN0.35\%}$ retrospective time for a) all clouds and b) precipitating clouds.